Hochschule Wismar
University of Applied Sciences
Technology, Business and Design
Fakultät für Ingenieurwissenschaften, Bereich EuI

Master Thesis

Analysis of Radar Data Applying Radar Imaging Techniques to Investigate Middle Atmosphere Radar Echoes

In partial fulfillment of the requirements for the degree of

Master of Engineering | Information and Electrical Engineering

Submitted on : 17. December 2019

Submitted By : Divakar Meganathan
Matriculation. Nr : 271572

Supervisor : Prof. Dr.-Ing. habil. Andreas Ahrens
Arbeitsbereich Nachrichten und Kommunikationstechnik
an der Hochschule Wismar

Second Supervisor : Dr.-Ing. Toralf Renkwitz
Leibniz-Institut für Atmosphärenphysik
an der Universität Rostock

Leibniz-Institut für Atmosphärenphysik Schlossstraße 6, 18225, Kühlungsborn

Abstract

Strong radar echoes occur in between altitudes 80 and 92 km in the mesospheric region, which is due to the occurrence of the polar mesospheric summer echoes. It is mainly due to the presence of ice particles (water vapor), free electron, turbulence and breaking down of gravity waves. In particular, the mesopause region exhibits cold temperatures during summer (reaches below 140 K) i.e. the coldest region in the atmospheric scale. Polar Mesospheric Summer Echoes (PMSE) use as a natural tracer for the crucial atmospheric behavior in recent decades. The study of these horizontal structures of the PMSEs was in this range extends up to several 10s of kilometres.

This thesis deals with the study of small-scale structures of PMSEs using high-resolution imaging techniques such as Capon and Maximum Entropy, which are implemented in MAARSY radar for MIMO and SIMO configurations. By implementing MIMO configuration, the angular resolution of MAARSY were increased and the resolution of the horizontal structures of PMSEs were reduced to a few kilometers (less than 1 km). The zonal and meridional wind were studied by considering background wind as homogeneous in nature. In summary, this thesis shows the importance of analysis with radar imaging techniques of MIMO and SIMO configurations for real time evaluation. Also, it shows the movement of horizontal structures of PMSEs to trace the small-scale structures.

Keywords: PMSE, gravity waves, turbulence, free electron, mesopause, Capon, Maximum Entropy, MIMO, SIMO, MAARSY, virtual antenna.

Contents

List of Abbreviations

RADAR RAdio Detection And Ranging

PMSE Polar Mesospheric Summer Echoes

MAARSY Middle Atmosphere Alomar Radar System

MSIS Mass Spectrometer Incoherent Scatter

MST Mesosphere Stratosphere Troposphere

VHF Very High Frequency

MF Medium Frequency

RI Radar Imaging

SIMO Single Input Multiple Output

MIMO Multiple Input Multiple Output

HPBW Half Power Beam Width

RTI Range Time Intensity

RTDI Range Time Doppler Intensity

JRO Jicamarca Radio Observator

NARL National Atmospheric Research Laboratory

DBS Doppler Beam Swing

LIDAR Light Detection and Ranging

NLC Noctilucent clouds

PMC Polar Mesospheric Clouds

UTC Universal Time Coordinated

KHI Kelvin-Helmholtz Instability

List of Figures

List of Tables

Chapter 1

Introduction

The study of atmospheric layers has played a significant role in the last couple of decades. The rise in pollution rate in the environment is due to the emission of toxic gas from the vast number of industries, automobiles, forest fires and some volcanic eruptions, which affect the climate and weather. This leads to the rise of temperature, seasonal variations and other natural phenomena over tropical, subtropical and even polar regions. Since each layer of the atmosphere is stacked over one another, the effect in one layer impacts the other layers too. The physical parameters of each atmospheric layer have to be analyzed to create a climate model [Mearns et al. 2003] for weather forecasting and other space science research.

The measurement technique of each layer varies due to several practical difficulties with increasing altitudes. For some altitudes, satellite mission are used to measure directly or remote sensing and for the lower altitude, the Situ measurement technique [Pielke 2019], hot air balloons, sounding rockets, radar, lidar, optical imagery are used. But each method has its advantages and disadvantages. Lidar and optical imagery are limited to weather conditions due to the presence of tropospheric clouds. In case of the sounding rockets, it provide high profile measurements which are very expensive in usage. The measurement of vertical velocity is limited with the hot air balloons due very high drift velocities prevailing with the wind. Radar, however has advantages to overcome some of these limitations, such as it can operate throughout the day and night in all sort of weather and atmospheric conditions.

The middle atmosphere ranges from 50 km to 120 km in altitude stacked with the stratosphere, mesosphere and lower thermosphere. The tropopause, stratopause and mesopause regions are characterised by temperature gradient inversion. It is the rate at which the temperature changes most rapidly in a particular location. The mesopause region in particular will exhibit an unusual dynamical behaviour such as breaking of gravity waves which leads to the deposition of momentum that causes turbulence. Particularly, the turbulence and wind estimation from the middle atmosphere are very rare to find. Still, the information is much needed to create a climate model to produce the physical process of the atmosphere. Moreover, the atmospheric density will decrease exponentially with increase in altitude. The strong echoes are easier to observe in mesosphere than in the troposphere and can be seen in Figure 1.1.

Most of the gravity waves are generated in the troposphere will gain amplitude through the stratosphere and finally break down in the upper mesosphere i.e. mesopause region. The effect of gravity waves at lower altitudes (10-15 km) maybe caused by the thunderstorms and jet-stream. Gravity waves can propagate both in horizontal and vertically upward directions. In extreme case, some of the gravity waves will reach the lower thermosphere [Becker and Vadas 2018]. Their oscillation period can vary between a few minutes to approximately the earth's intrinsic period but can be slightly shorter or longer. The change in energy and momentum results in adiabatic cooling and causes the temperature to fall below 140 K in the mesopause at about 85 km in altitude [Witt et al. 1965; Lübken et al. 1993]. This cold temperature below the frost point of water vapour leads to the phenomena of formation of ice crystals in this region. The temperature variation in summer and winter is shown in Figure 1.1. This plot shows the temperature profile at the polar coordinates $[69.30°N, 16.04°E]$ from the empirical MSIS model (Mass Spectrometer Incoherent Scatter) [Picone et al. 2002]. During summer the temperature falls below the frost point of the water vapour. This ice formation is observed for a longer time which is called Noctilucent clouds (NLC). Due to the presence of ice clouds and incident solar radiation charging occurs which allows strong VHF radar echoes [Rüster et al. 1983; Balsley et al. 1983].

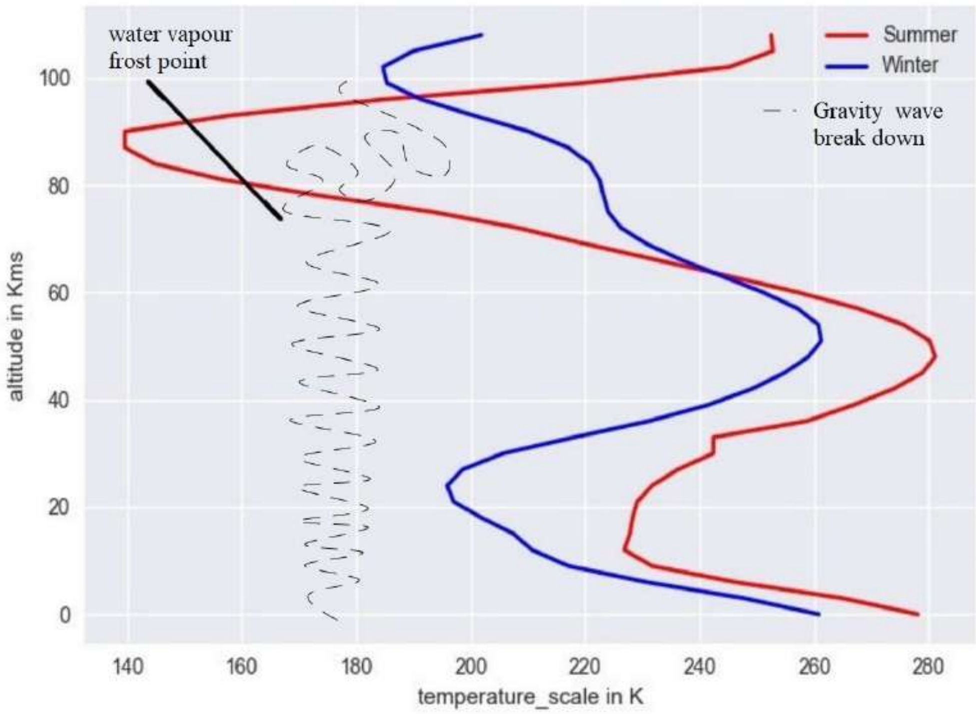

Figure 1.1: The neutral temperature profile up to 130 Km for the winter and summer season derived from NRLMSISE-00 Atmosphere Model 2018. Summer shows much lower temperature than winter, the black line indicates the water vapour frost point and the dashed line indicates the propagation of gravity waves and breaking down at mesopause region. [NASA]

1.1 Motivation

The study of Polar Mesospheric Summer Echoes (PMSE) are done with the conventional measurements techniques such as single beam, multi-beam DBS, FCA has evolved over the period. To improve the resolution with effective analysis of the small scale structures of PMSE were carried out by imaging. The imaging techniques have been used effectively in recent years in mesosphere stratosphere troposphere (MST) radar group. Imaging radars can produce a visual representation of the geometric distribution of the electromagnetic scattering properties of an object under observation. The imaging technique involves interferometry, which depends on the phase difference of the received signals to locate the scattering structure. Using the multiple receivers angular position of the scattering structures can be derived for each range bins as well as for the frequencies bins. There are several limitations due to the generation of PMSE, motion of the horizontal structures and its evolution over time cannot be separated and this raises space time ambiguity problems.

The first application of this imaging technique was performed by [Kudeki and Sürücü 1991] for the observation of Equatorial ElectroJet (EEJ) above the Jicamarca Radio Observatory which is a large incoherent scatter radar in Peru. In this experiment, Fourier based technique was used as a generalization of the post-statistic steering method to perform wind field measurements. This post-set beam steering method was developed for image processing but there was side lobe domination. To suppress these sidelobes [Capon 1969] proposed a technique to reduce the interference signal. Also from the work of [Hysell 1996], applying maximum entropy method in imaging technique offers greater resolution than Capon and Fourier techniques.

MST radar receivers need to offer a higher dynamic range. These MST radars have capabilities such as working actively throughout the day and night in all weather conditions. In this thesis, the Middle Atmosphere Alomar Radar Systems (MAARSY) on an island in Northern Norway is used to investigate small scale PMSE structure and dynamics. Furthermore, small scale structure width of PMSE are of large interest to further study their formation and evaluation. As the angular resolution is given by the radar beam width and its antenna array size, the imaging technique may overcome these limitations.

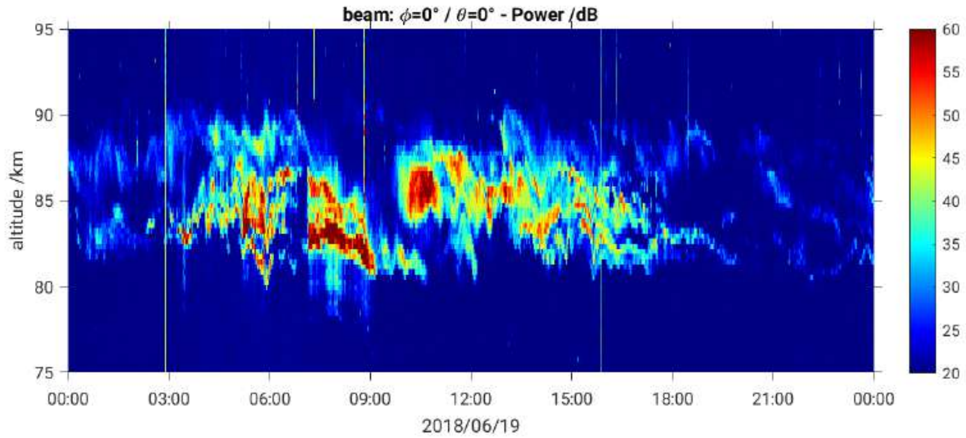

Figure 1.2: Detected echo power for vertical beam of Doppler Beam Swinging (DBS) of the PMSE structure altitude and time. Echoes occur between 80 km and 90 km altitude as shown in this example for 19^{th} June 2018 from MAARSY.

1.2 Radar measurements in middle atmosphere

RADAR is an acronym for RAdio Detection And Ranging. Radar has been developed in the early 20^{th} century with general application since world war II for surveillance and military purposes. Radars can operate in a variety of frequency bands ranging from a very few millimetres to several kilometres. Radar pulse can be reflected or scattered due to the change in the electromagnetic refractive index of the atmosphere. The distance travelled by the pulse from the transmitter (radar) and the target can be calculated by the time duration between the transmitted pulse and the received pulse. We know that an electromagnetic wave can travel at the speed of light in case of vacuum and approximately also for "normal" air (299 792 458 m/s). In the case of the ionosphere, the propagation and velocity depends on the electron density, frequency and polarization.

Band	Nomenclature	Frequency	Wavelength
MF	Medium Frequency	300 - 3000 kHz	1 km - 100 m
HF	High Frequency	3 - 30 MHz	100 - 10 m
VHF	Very High Frequency	30 - 300 MHz	10 - 1 m
UHF	Ultra High Frequency	300 - 3000 MHz	1 m - 10 cm
SHF	Super High Frequency	3 - 30 GHz	10 - 1 cm
EHF	Extremely High Frequency	30 - 300 GHz	1 cm - 1 mm

Table 1.1: Radio frequency bands

The radar observations are typically classified by the frequency ranges such as several MHz to GHz. The Ultra High Frequency (UHF) range in GHz used for the meteorological radar and in MHz for wind profilers. **MST** stands for Mesosphere Stratosphere and Troposphere, these radars are operated in VHF frequency range to be able to obtain echoes from the lower troposphere up to the higher mesosphere. Doppler radars operating from 40 MHz to 55 MHz are frequently used for the investigation of various dynamic processes in the middle and lower atmosphere. The MST radar has the ability to detect coherent backscatter signals from 1 km to 100 km. These radars are used to investigate the 3D winds(zonal and meridional directions), turbulence and other dynamic behaviors of the atmosphere with the help of imaging techniques using interferometry [Hocking et al. 2016b].

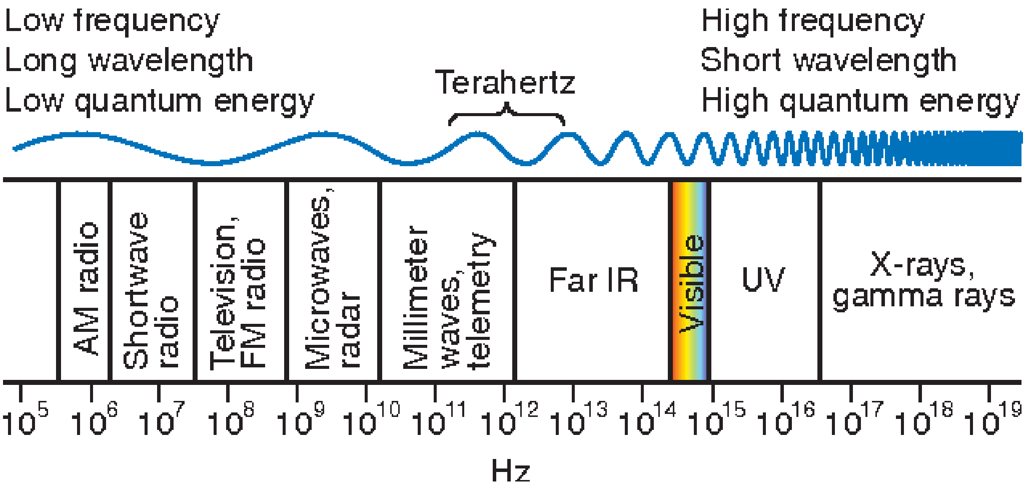

Figure 1.3: The electromagnetic spectrum.
[Fitch and Osiander 2004]

1.3 Scattering mechanism of radar emissions

Scattering of the radar signal from the plain air (undisturbed) is because of the change in the electromagnetic refractive index [Smith and Weintraub 1953].

$$n = 7.76 \cot 10^{-5} \frac{p}{T} + 0.373 \frac{e}{T^2} - \frac{N_e}{N_c} \tag{1.1}$$

where p = 0.05 mbar is the total pressure of the water vapour , T = 150 K is the temperature, e is electron density, $N_e = 3000 cm^{-3}$ is the electron number density and $N_c = 2\pi \frac{\epsilon_0 m_e}{e^2} f^2$ is the critical electron number density, $\frac{e}{p}$=3ppmv , ϵ_0 as permittivity of free space, m_e electron mass, e is electron charge, f is wave frequency.

The region of our interest in the mesopause region may not be consider neutral due to the breaking down of gravity waves, turbulence and presence of ice particles. The free electron are stacked in the ice layers where the diffusion (mobility) of the electrons will be reduced which may cause dispersion of the radio signals. Hence in mesosphere, radar backscattering occurs due to the higher Schmidt number. The Schmidt number is defined as the ratio of momentum diffusivity and mass diffusivity of free electron. Medium frequency (MF) radar backscatters occur due to the free electron and for very high frequency (VHF) backscatters occur due to the larger electron density without the enhancement of Schmidt number. We may observe different scattering mechanisms such as Thompson scattering and Fresnel or Bragg scattering. Thompson scattering it is due to the motion of electrons, ions and therefore also related to temperature. Bragg scattering is caused by the structure at half of the wavelength of the radar signal [Wikipedia contributors 2019]. With the constructive interference of the scattered signal due to incident solar radiation, the free electron and plasma are generated.

1.4 Observation of PMSE layers

During the period of end of May, the occurrence of PMSEs begins followed by the month of June and July with stronger echoes characterized by signal to noise ratio (SNR) larger than 10 dB with the occurrence rate of 70% to 90% [Hoffmann et al. 2003]. Occurrence rate gradually decreases from the beginning of August month. The study of horizontal layers can be characterised as follows.

1.4.1 Multiple layers of PMSEs

The remarkable feature of all PMSEs is that the echoes often occur in the form of two or more distinct layers which may exist for a period of up to several hours. Until now, the layer mechanism of the multiple layers has not been investigated in depth [Hoffmann et al. 2003]. The multiple layers may be the correlation between two echoes power and the squared vertical gradient of the temperature. An approach was proposed first by [Hoffmann et al. 2003] to perform an experiment but the result was biased. We see the vertical gradient of the temperature scales down in the mesopause region were the temperature falls below 140 K.

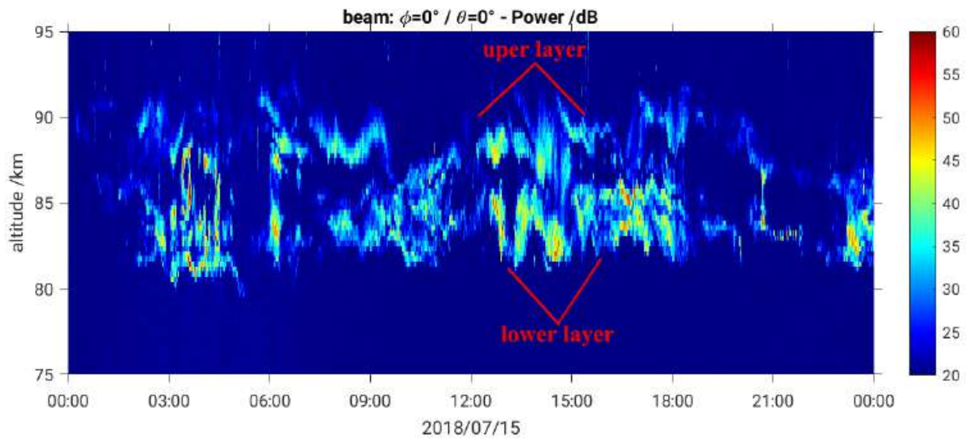

Figure 1.4: The dual layer for the PMSE corresponding to 15^{th} July 2018. The red line indicates the two separate layers of enhanced echoes at different altitudes.

A new theoretical approach was proposed to study the microphysical structure for the dependency of the PMSE. The PMSE structure varies due to the charged ice particles and the size of the aerosol. The multiple layers of PMSE structure arise due to the influence of the temperature and wind variation caused by the longer gravity waves. But the theoretical results were biased. So an experiment was performed with VHF radar above 85 km on 11^{th} July 2001 at 8:00 UT. The plots can be viewed in [Hoffmann et al. 2003] in Figure 8. shows the wavelet power spectra from the verticle profiles of zonal and meridional winds are derived from ALWIN VHF radar. To detect the multiple layer structure of PMSE, a simple method was applied for the different individual vertical beams. The center height for each layer can be estimated with simple weighted mean of the two vertical beams as expressed below [Hoffmann et al. 2003].

$$H_{max} = \frac{\sum h_i \cdot SNR_i}{\sum SNR_i} \tag{1.2}$$

where h_i is the height of the incident wave, i is the incident wave. The multiple layers of polar mesospheric summer echoes (PMSE) are mainly caused due to the layering of charged ice particles which is ultimately due to the cold phase of the large scale gravity waves. This analysis helps us to study the dual layer structure of the PMSE.

1.4.2 Layer thickness of PMSE

PMSE appears in thin layers from 0.1 to 2 km in thickness at the altitude between 80 and 90 km. They often occur in dual or multiple layers and also in "patchy" structures caused by dynamics (including waves), the temperature profiles and their horizontal structures [Hoffmann et al. 2003]. Although the layers can move up and down rapidly, they often seem to move downward over a longer period of time in approximate hours. PMSE occur in the same season as optically visible Polar Mesospheric Clouds (PMC). PMSE are usually small sized particles and thus precursor of PMC. This might be due to the growth of particles slowly precipitating [Siskind et al. 2018; Sommer and Chau 2016].

1.4.3 Aspect sensitivity

Aspect sensitivity is one of the properties of radar echoes that can potentially explain a lot about the physics of the scattering process and the nature of scatters. The aspect sensitivity dependence on the angle of the incident wave to the target and the target's shape modifying the echo strength (reflectivity). In general, a strong back scatter signal power decreases with increasing beam tilting angle [Rapp and Lübken 2004].

The intensity of the aspect sensitivity is usually expressed as the half width of tilting angle θ as observed by [Hocking et al. 2016a]. So, a larger value of the θ leads to a smaller aspect sensitivity and vice-versa. The first measurement of aspect sensitivity for PMSE was done by Czechowsky in 1988. The Aspect sensitivity with θ between $2°$ to $10°$ was found small. The structure of the aspect sensitivity and spectral width in the upper layer of the PMSE are more turbulent. In contrast, they appeared to be non-turbulent (specular) in the lower layer.

Most of the PMSE seem to have a narrow spectral width and a strong aspect sensitivity. A small portion is caused by the turbulence at an altitude of 86 km. Recent experiment by Sommer and Chau [2016], small-scale irregularities were observed showing isotropic scattering. Since the structure more often organized in horizontal patches, the aspect sensitivity is not the main source for the occurrence of polar mesospheric summer echoes.

In this thesis, the analysis of the PMSE structure are used as a target in the middle atmosphere which are focused using radar imaging techniques. This work is structured as follows: In Chapter 2, describes the different measurement techniques in the middle atmosphere using MAARSY radar. the Chapter 3 describes the various radar imaging techniques like Fourier, Capon and Maximum Entropy along with their underlying mathematical formulations. Chapter 4 describes the investigation of

PMSE by imaging techniques that have been applied to extract the images from raw data. Chapter 5 discusses the results of the imaging method for SIMO and MIMO configuration. A brief summary of the thesis work is given in Chapter 6.

Chapter 2

Radar measurement techniques

Radar backscatter signals can be analyzed with the echo power or Signal to Noise Ratio (SNR) and the spectral shape. The MST radar have been used to measure wind speed, the direction of arrival and also to estimate the energy dissipation rate from the backscatter signals. Different measurement principles and techniques such as single beam, multi-beam, Doppler Beam Swinging (DBS), Full Correlation Analysis (FCA) were developed to derive the parameters of the atmosphere from the backscatter signal.

2.1 Doppler beam swinging

Doppler Beam Swinging (DBS) modes are widely used for the wind profile estimation. DBS uses different oblique beams into individual pointing direction of the radar, which are interleaved in order to measure the radial velocity along these directions. The vertical velocity can be obtained directly from the vertical pointing beam and can be used to improve the horizontal wind estimates. The accuracy of the DBS wind measurement depends on several factors such as total number of beams used (minimum of 3 beams but it can even extend up to 20 or more number of beams), zenith angle of the off-vertical beams and the atmospheric condition. For example, the 5 beam configuration can give a more accurate result compared with the 3 beam configuration, in particular, the small scale variation in vertical wind direction [Woodman and Guillen 1974].

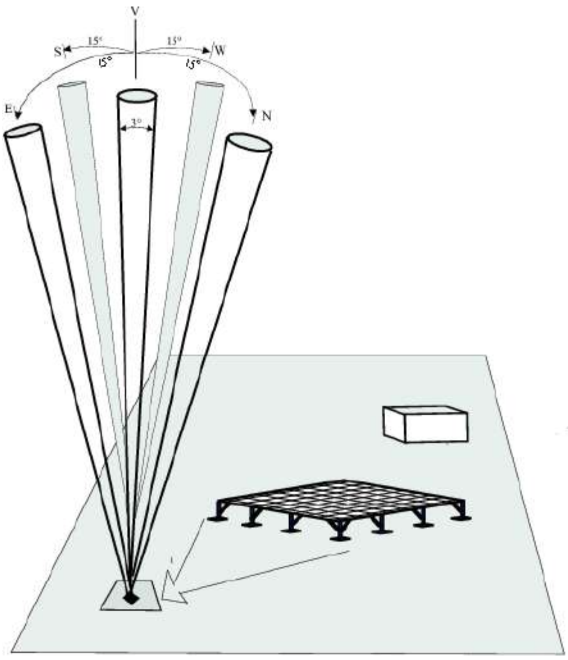

Figure 2.1: Five beam DBS profiler antenna pointing [eco 2013].

The accuracy for the horizontal wind estimation increases with increasing zenith angles of the off-vertical beams. But the precision of the DBS may vary due to the in-homogeneity of the wind and turbulence. The radial velocity in SNR is reduced for larger zenith angles. For example, for a small change in the pointing direction, the radial velocity of the wind changes drastically. The radial velocities at different regions of the sky can be determined by comparing the respective directional beams with a vertical beam at the center.

2.2 Radar Interferometry

Interferometry relies on the fact that the radar system can measure the phase information of the received signal. The phase difference of the received signals gives us the information of the angle of arrival from the different sources. For the imaging technique, interferometry uses the phase information of the different sources and are stored in each pixel for different antenna positions. By correlating the pixels for the different antenna we can derive the 2D image of the two sources. There are two different modes, mono static and bistatic. If there are two different radar systems in space, it is called as bistatic mode, on the other hand, a mono static mode is when the antenna transmits and receives in the same location.

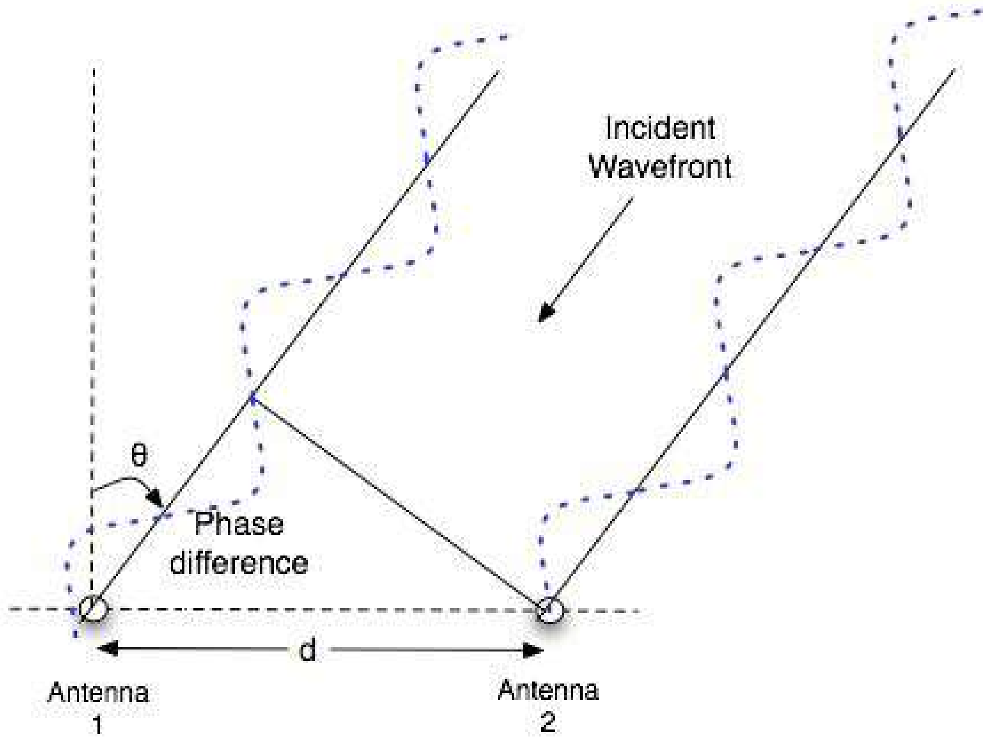

Figure 2.2: Radar interferometry with two antenna separated at distance d in the same plane. since, the incident wave reaches the antenna 1 and have to travel for the 2π distance [Wikipedia contributors 2018]

The separation between the two antenna determines the small difference in phase of backscatter signal of the source. For example, human ears measure a phase difference at low-frequency sound waves, one single ear is not very good at determining direction. Using the pair of our ears and measuring the phase difference of the signal at one ear and another ear, we can tell roughly from which direction of the sound. When the sound wave travels in one direction i.e. the ear closer would detect sooner and the other would detect a little late. The extra distance travelled by the wave from one to the other ear gives us the phase difference from which we can roughly predict the direction of sound.

The same principle is used in radar systems, for a given offbore sight position of the scatterer, a phase difference can be measured between the separated antennas. Pulse radar system measures the range information precisely. The range resolution depends on the pulse width. The range resolution can be improved by using either a shorter pulse. By measuring the phase difference of the echoes the directional information can be derived. With the range and directional information, the exact location of the echoes can be determined in the polar coordinates. From the echoes information with the phase difference it is possible to formulate two images of the same source. Then these two images are correlated to acquire the desired structure precisely. The scatters are not constant due to atmospheric dynamics such as turbulence and other behaviours. The echoes might not be consistent with space and time to derive acceptable phase difference information or else this may lead to phase ambiguity.

2.3 MIMO radar system

MIMO radar system is an innovative technique in which MIMO stands for Multiple Input Multiple Output. It is a system of multiple antennas for transmission and reception. Each transmit antenna radiates a separate waveform independently of the other transmitting antenna and each receiving antenna can receive these signals. Due to the different waveform the echo signals can be reassigned to each of the single transmitters. With MIMO we can derive a large scale area of the virtual field, which provides the full opening of the virtual aperture. Since MAARSY can be operated with SIMO and MIMO configurations, for example, let us consider T as the total number of transmitters and R as the total number of receivers. The total number of virtual fields V_f is given by the product of T and R.

$$V_f = T \times R. \tag{2.1}$$

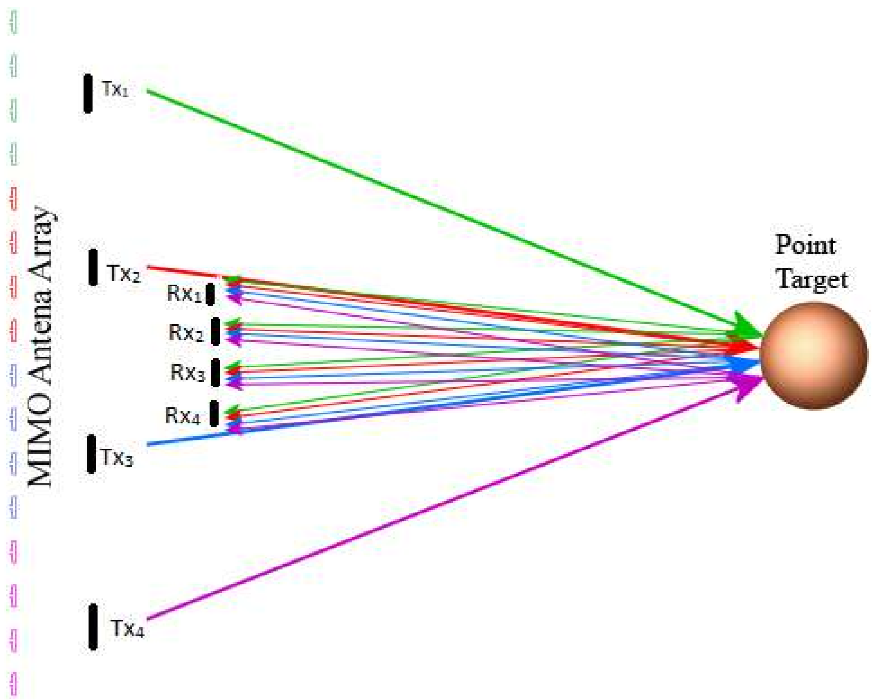

Figure 2.3: MIMO virtual antenna array

Figure 2.3 shows a point target with MIMO configuration. The MIMO radar is further classified into monostatic and bistatic. If the MIMO radar antennas are placed side by side, it is called monostatic MIMO. MIMO radars with widely separated antennas are called bistatic MIMO.

2.4 MAARSY radar

The Middle Atmosphere Alomar Radar System (MAARSY) located on the northern part of Norwegian islands called Andøya ($69.30°N, 16.04°E$). MAARSY is a monostatic radar with the transmitters and receivers located in principally the same location. MAARSY consists of an active phased antenna array. Most MST radars are operated in the lower VHF ranges, for example between 40 MHz to 55 MHz. A short demography of the MST and MU radar for the VHF band are explained as follows, the MST radar and MU radar are employed in early 1980s. The first observation was done at Jicamarca in 1977 [Fukao et al. 1980] to observe the radio wave scattering from tropical mesosphere. Later the Equatorial Atomosphere Radar

(EAR) are observed form Sumatra, Indonesia (47.0 MHz) [Yamamoto et al. 2003]. Most recently Program of the Antarctic Syowa radar (PANSY) at Syowa, Antartica (47.0 MHz) is under construction [Sato et al. 2014]. The list of other MST radar around the world were names as follows, MAARSY, Norway (53.5 MHz), MU radar, Japan (46.5 MHz), Gadanki radar, India (50 Mhz), Davis radar, Antarctica (55.0 MHz). The basic parameters of MAARSY is shown in table 2.1.

Figure 2.4: The view of the MAARSY site located on the northern part of Norwegian island Andøya (69.30°**N**, 16.04°**E**) [Renkwitz et al. 2013].

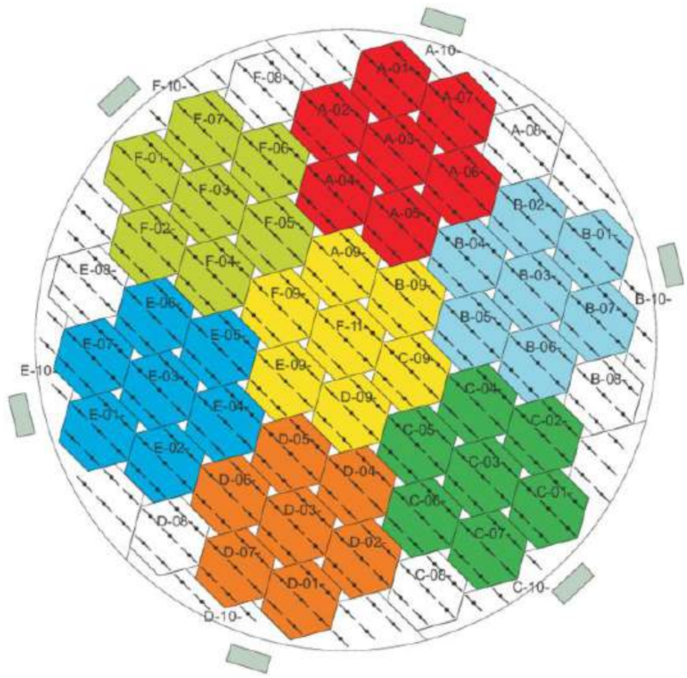

Figure 2.5: Sketch of the MAARSY radar antenna array in colored subgroups mark the MAARSY343 subarray with 7 anemones [Renkwitz et al. 2013].

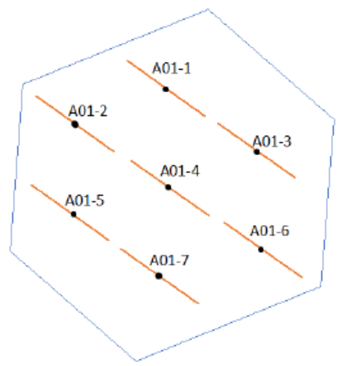

Figure 2.6: Single hexagon with seven cross antennas for the selected hexagon A-01 out of the anemone A

The construction of the MAARSY radar started in 2008 as a significant improvement to the earlier ALWIN MST radar at the same location. The number of transceiver modules were gradually increased from 196 transceivers in spring 2010 to 343 transceiver modules installed in November 2010. Finally, 433 transceiver modules were finished after six months in May 2011 [Latteck et al. 2012].

2.4.1 MAARSY antenna array

The MAARSY can be operated in different radar working modes. Since MAARSY is constructed in the Active phased antenna array, the transmitter and receiver modules can be individually controlled to change the phase offset and the output power. This results in a high degree of beamforming and steering the beam in a particular direction. The complete 433 antennas were formed into an array of 55 subgroups for receiving. In particular seven antennas are grouped into one subgroup called a hexagon. A total of seven hexagons are arranged to form an anemone. These hexagons are arranged in an equilateral triangle grid forming a circular area of approximately 6300 m^2.

Description	
Location	Andenes, Norway (69.30°N, 16.04°E)
Operating frequency	53.5 MHz
Allocated frequency	4 MHz
Frequency swiftness	52.5 MHz - 54.5 MHz
Peak power	$\sim 800kW$
Max duty cycle	5%
Pulse repetition frequency	$\leq$ 30 kHz
Pulse width	$\geq$ 0.33 µsec
Sampling resolution	$\leq 50\ m$
Transmitted waveform	Single pulse, Complementary, Barker codes
Pulse shape	Square, Gaussian shaped, Trapezoid
Antenna array	433 three element Yagi
Total area	$6300\ m^2$
Half power beam width	3.6 °
Directive gain	max 33.5 dBi
Beam direction	arbitrary at zenith angle $<$ 30 °
Receiver channels	16

Table 2.1: General parameters of MAARSY

The total area is divided into 6 symmetrically spaced anemones (A-F) Figure 2.5 and each area is composed of 7 antennas which can be illustrated as hexagons and the seven hexagons were called as one anemones, [Latteck et al. 2012] it allows to perform the different experiments in the different antenna configuration. The experimental parameters for MIMO configuration will be given in the upcoming section. The various separated receiving channel signals allow spatial domain interferometry applications [Woodman 1997; Palmer et al. 1998]. A change in the frequency for each separate transmitted pulse offers interferometric applications in time domain.

2.4.2 MAARSY experimental configuration

To upgrade the performance of this imaging experiment, we have implemented coherent MIMO and SIMO configurations in MAARSY radar system [Urco et al. 2019]. We know the operation of SIMO uses a single transmitting antenna and multiple receiving antennas, MIMO uses multiple transmitting and receiving antennas respectively, both these techniques use antennas which are separated spatially. Also, the signal from each transmitting and receiving path are coherent and can be combined to form a larger virtual receiving antenna. The virtual receivers are equal to a simple multiplication of the transmitters and receivers.

Depending upon the transmitting and receiving antenna configuration, some of the virtual receivers were not used in the operational mode. In this experiment, we consciously select the transmitting and receiving antenna to get the virtual receivers without overlapping each other. Figure 2.7 shows the 15 hexagons used for reception and the three anemones Figure 2.7(b, d, f) used in transmission, Figure 2.7 (d) shows the resulting virtual receivers.

To achieve the transmitter diversity between transmitting modules we can either implement code, time and polarization. Code diversity was highly recommended in the radio astronomic observation, which is not sensitive to temporal correlation or polarization of the target of interest. Unfortunately code diversity cannot be implemented in MAARSY radar.

Description	
Operating frequency	53.5 MHz
Pulse repetition frequency	1 KHz
Transmitted waveform	Complementary 16
Number of Transmitters(beams)	5
Transmitter Diversity	time
Transmitter interleaving	2ms
Number of coherent integration	8
Number of FFT points	16
Number of incoherent integration	128
Range resolution	300 m
Receiver channels	16

Table 2.2: Configuration of MAARSY for MIMO experiment

Since the target is unsophisticated in nature, time diversity is used such that the temporal correlation is less than the time between the transmitter.A better resolution of the Polar Mesosphere Summer Echoes (PMSE) can be achieved by using which has longer correlation time [seconds and above]. The effective time separation between transmitters is 0, 2, 4 ms between the pairs.

A short explanation for the visibility between SIMO and MIMO is shown in the Figure 2.7. The MIMO configuration uses 45 transmitting channel which results in number of virtual receiver antennas.Figure 2.7 (d).Figure 2.7 (e) shows that the antenna aperture for MIMO is very larger compared to SIMO nearly 50%. The aperture is enlarged by the distance between the individual transmitter subarrays, which is also evident from the visibility of MIMO and SIMO as shown in Figure 2.7 (b) and Figure 2.7 (e) . The Point Spread Function (PSF) describes the impulse response of the imaging system to a point source or point object.

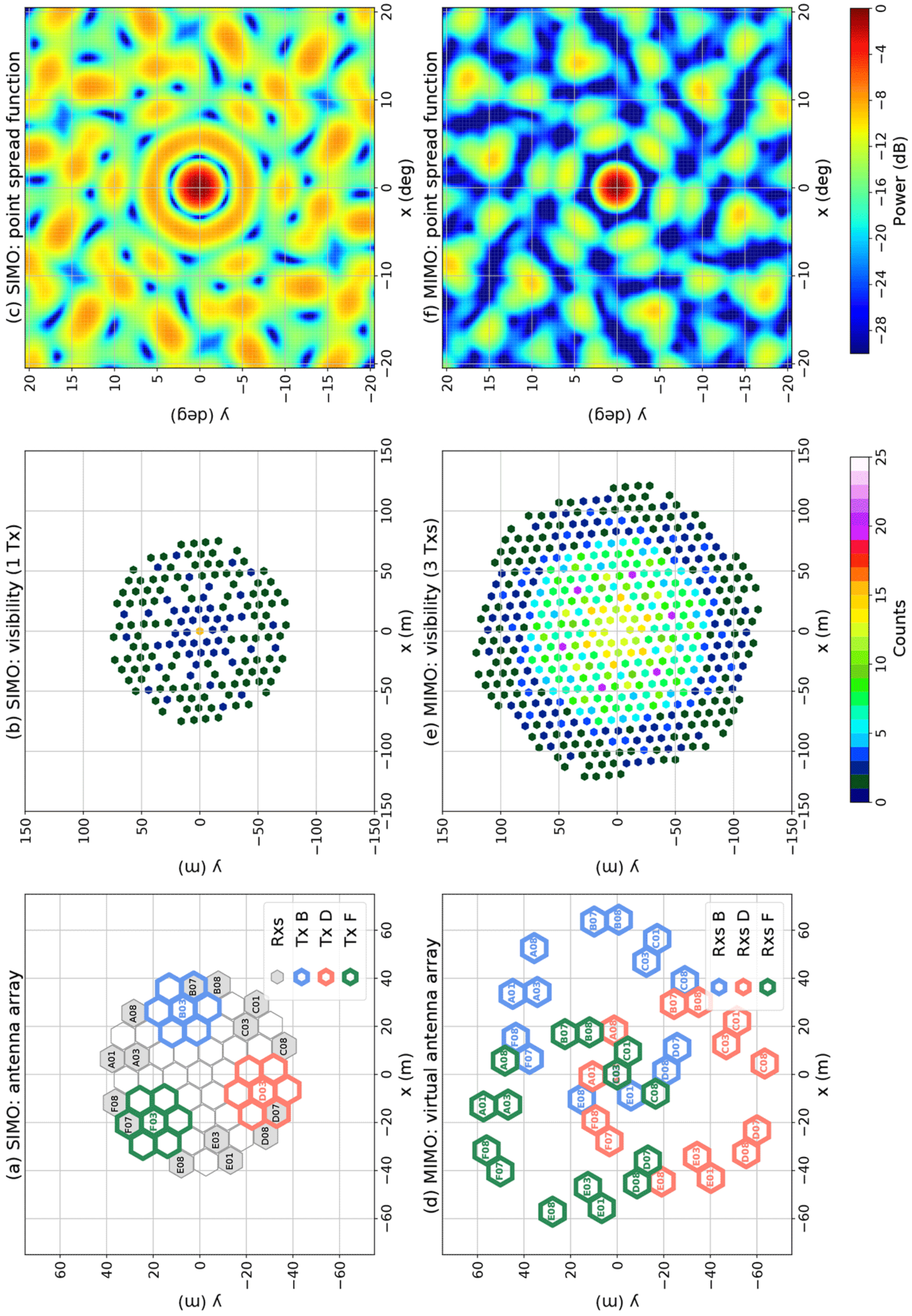

Figure 2.7: MAARSY antenna configuration for SIMO and MIMO. (a) The grey shaded 16 hexagons are used for reception and three colored anemones were used for transmission. (b) SIMO is the visibility samples. (c) Point spread function of SIMO.(d) The transmitting antenna position for MIMO. (e) MIMO is the visibility samples. (f) Point spread function of MIMO. The shown antenna configuration is similar to [Urco et al. 2019]

The width of the impulse decreases with increasing resolution of the point source and vice versa. Figure 2.7 (c) and Figure 2.7 (f) show the PSF for the SIMO and MIMO respectively, as expected that the half power beam width (HPBW) for MIMO is 50% lesser (2.4°) than that for SIMO (3.6°). The smaller beam width allows the imaging system to analyze the image pixels at very small scales. Moreover in MIMO configuration the side lobes are strongly reduced, thus in results larger visibility.

Chapter 3

Radar imaging techniques

3.1 Coherent radar imaging

Coherent radar imaging is a term which can be used to describe various array processing algorithms. Signals from each sensors are processed to focus the receiver sensitivity in a particular direction [Johnson and Dudgeon]. This development is an outgrowth of the Radar Interferometric (RI) techniques [Woodman 1997] and shows the connatural ambiguities between temporal and spatial dimensions. Imaging techniques can create the instantaneous picture of the atmosphere within the radar beam.

Similar to the description in Chapter 1 imaging techniques are used to create the digital picture of the reflected surface or the brightness distribution, within the range of the radar beam [Kudeki and Sürücü 1991]. It can be bisected into vertical and horizontal cuts, where the vertical maps can be created by a standard gating procedure in accordance to the pulse width by the atmospheric radar. The horizontal maps of the brightness distribution have to perform differently via beam steering. Since the vertical beam steering is limited to a small number of directions using phased array antenna. This method of sampling the brightness distribution can not be analyzed for the tiny structure and the dynamics of the atmosphere.

To steer the beam in a particular direction the signals from each antenna elements are combined with certain phase shifts. This principle has been implied to the imaging technique from a finite set of receiving antenna array with various conventionality. Normally the brightness in the direction of the wavenumber vector $\vec{k}$ is estimated by combining the signal from n receivers. This configuration is sketched in Figure 3.1. the wavenumber vector $\vec{k}$ is given by.

$$\vec{k} = (\tfrac{2\pi}{\lambda})[\sin\theta\sin\phi \ \sin\theta\cos\phi \ \cos\theta] \qquad \text{is a column vector.}$$

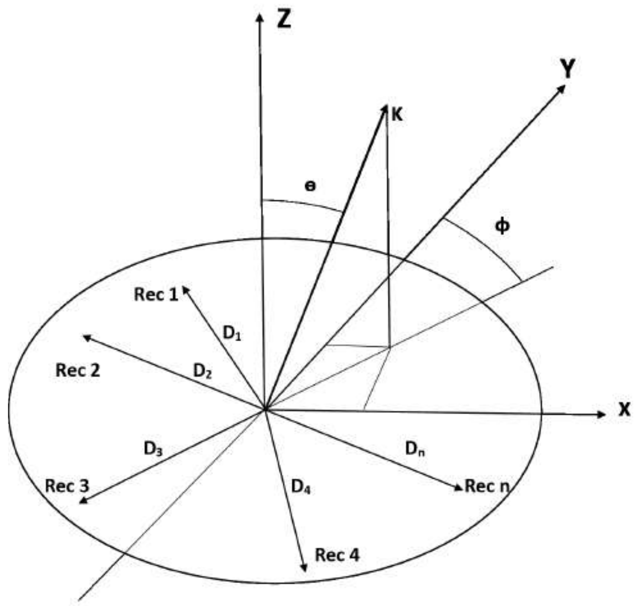

Figure 3.1: General configuration of interferometric model with n receiver channels. The vector $\vec{k}$ represents the zenith and azimuth angles θ and ϕ, the vector D_i for the various receivers i [Palmer et al. 1998]

This target steering vector is formed by the cross product of the vector representation of Doppler frequency and the vector representation of the zenith and azimuth angles θ and ϕ. For understanding only the azimuth angle is considered. The Doppler frequency offset vector is a complex phase rotation.

$$F_d = e^{-2\pi \cdot n \cdot F_d} \quad for \qquad n = 1, ...N - 1. \tag{3.1}$$

[Palmer et al. 1998].

The spatial angle vector is also phase rotation vector.

$$A_\theta = e^{-2\pi d \cdot m \cdot sin(\theta/\lambda)} \tag{3.2}$$

[Palmer et al. 1998].

The horizontal map of the brightness could be obtained by varying the $\vec{k}$ over the region of the sky appropriately. The wavenumber vector $\vec{k}$ is varied within the analysis as a kind of post beam steering (by software) and the resolution of the horizontal map depends on the length between the antenna and the n signal are combined.

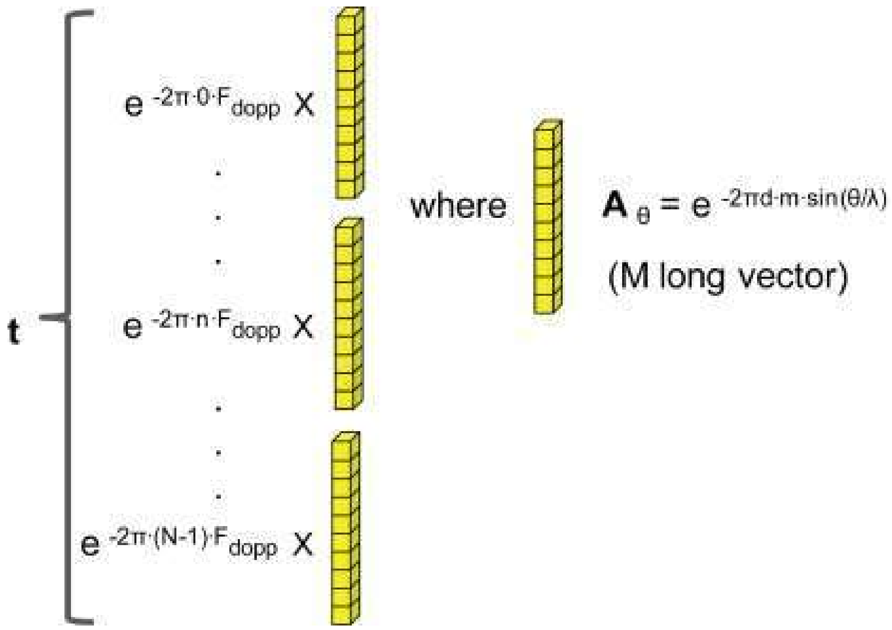

Figure 3.2: Steering vector t = f(Angle, Doppler) m=1,....M-1, for given angle of arrival θ and wavelength λ [Parker and Corporation 2011]

Let s(t) be a column vector containing the signal from n receivers. The goal is to find the optimum method to combine elements of the received signals s(t). We will choose a simple linear filter to combine the signal from the elements. The column vector constant coefficient is denoted by *w*, and the output of the filter y(t) [Palmer et al. 1998].

$$y(t) = w^H \cdot s(t) \tag{3.3}$$

where H is the Hermitian operator (conjugate transpose). It is well known that w mainly depends on the wavenumber vector $\vec{k}$. The autocorrelation function of *y(t)* is calculated by.

$$C_y(\tau) = y(t+\tau)y^*(t) \tag{3.4}$$

Then after the applicable substitution, the autocorrelation function has a matrix format shown in Figure 3.3.

$$C_y(\tau) = w^H R(\tau) w \tag{3.5}$$

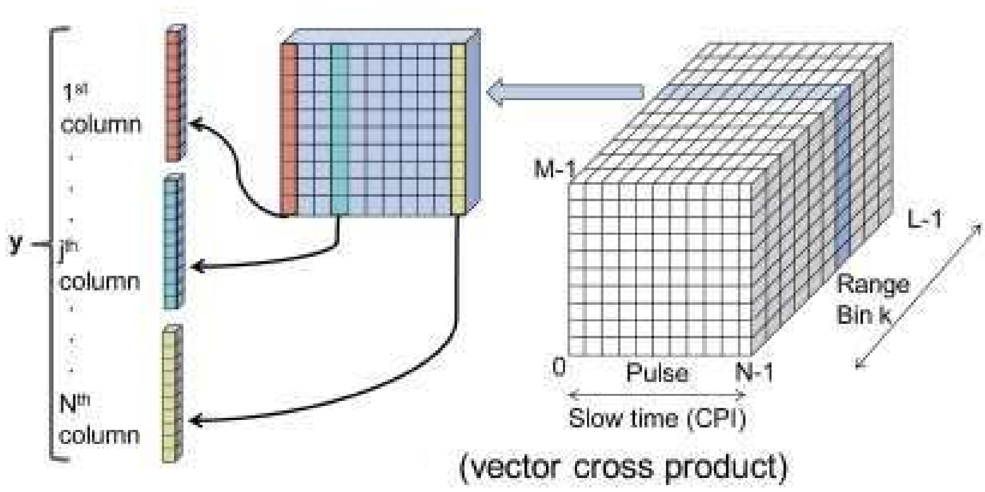

Figure 3.3: $C\tau$ is a Covariance matrix [Parker and Corporation 2011]

where C(τ) correlation matrix of s(t). After taking the Fourier transform and regularizing the matrix, we obtain the brightness distribution, which mainly depends on $\vec{k}$ is shown below [Palmer et al. 1998].

$$B(\vec{k}, f) = w^H V(f) w \tag{3.6}$$

The normalized cross-spectral matrix of the n receiver channels was formulated as V(f) as shown below.

$$V(f) = \begin{bmatrix} V_{11}(f) & V_{12}(f) & \cdots & V_{1n}(f) \\ V_{21}(f) & V_{22}(f) & \cdots & V_{2n}(f) \\ \vdots & \vdots & \ddots & \vdots \\ V_{n1}(f) & V_{n2}(f) & \cdots & V_{nn}(f) \end{bmatrix} \tag{3.7}$$

Where V_{ij} is the normalized cross-spectrum of the signal from the receivers i and j, which is called a visibility spectrum [Kudeki and Sürücü 1991]. By the normalization of each frequency, we obtain the following equation.

$$V_{ij}(f) = \frac{C_i(f) \cdot C_j^*(f)}{\sqrt{(|C_i(f)|^2)(|C_j(f)|^2)}} \tag{3.8}$$

Where $C_i(f)$ is the Fourier transform of the coherently detected signals from various receiver i. The amplitude of V_{ij} is typically termed the coherence. It should be stressed that V(f) has a dependence on temporal frequency f. Therefore a separate estimate of brightness distribution should be calculated for each Doppler velocity. It is essential to determine the suitable weight vector (w) to estimate the brightness in the direction of $\vec{k}$.

3.2 Fourier beam forming

Fourier based imaging is one of the earliest and most exciting approaches by Briggs 1973. The Fourier transform of the complex electric field is recorded by the large MF radar in a total of 89 antennas in the field. They cover a space of 1×1 km, to produce an instantaneous image of the brightness pattern over the whole sky. To achieve the angular brightness pattern, they need to perform the Fourier transformation of the spatial autocovariance function of the ground electric field, which is mostly done by the radio astronomy. From this approach, the visualization of the autocovariance function is found to be an intricate amplitude pattern across the sky rather than a simple brightness pattern [Hocking et al. 2016a].

At early attempts, sky image maps were produce by steering the beam consecutively in 360° of azimuth for the various elevation. To steer the beam in a particular direction in the sky, a proper phase shift should be introduced to each antenna. Therefore, constructive interference occurs in one direction and cancels out in other direction, i.e. beamforming. This method can also apply the received raw data, resulting in post statistic beam steering [Kudeki and Sürücü 1991; Woodman 1997].

$$W_F = \begin{bmatrix} e^{j\vec{k}\cdot D_1} & e^{j\vec{k}\cdot D_2} & \dots & e^{j\vec{k}\cdot D_n} \end{bmatrix}^T \tag{3.9}$$

By substituting the W_F in Equation 3.6, we get the brightness distribution. But this method has a flaw of having many side lobes. To overcome this Capon has introduced a method to choose the proper weight of the antenna.

3.3 Capon method

Even though the Fourier beamforming has shown results, the side lobes makes the resolution of image poor. In order to overcome this drawback, Capon has developed a sophisticated algorithm especially for the atmospheric reading, i.e. radio astronomy, seismic exploration and acoustic array processing. Capon's method which can also be referred as the minimum variance method, adaptively chooses the nominal weight between the antenna receivers. At early stages, this method was designed for the two-dimensional imaging for subterranean using the signal obtained from a seismic array [Capon 1969].

The resolution of the Fourier imaging is limited by the frequency response of the weight vector. Since the weight vector has the phase difference information, the magnitude response will be in standard form as Sinc function, which can quickly identify the main lobe and side lobe parameters. So one should use the best value for weight vector w, which could improve the resolution and suppress the side lobes [Capon 1969]. Hence idea was proposed by Capon to choose and appropriate weight of the W_F.

Adaptive beamforming is widely used in array signal processing for enhancing the desired signal by suppressing the interference and the noise at the output array of the antenna (sensor). On comparison with the independent data beamformers, the adaptive beamformers have a better resolution and much better interference rejection capability. However, the adaptive beamforming is somewhat sensitive to the steering vector mismatches, which will reduce the performance of the adaptive beamforming severely. The cause of the steering vector mismatches in the practical application includes Direction Of Arrival (DOA) errors and also imperfect array calibration or damaged antennas.

The primary aim is to find the weight vector W_F which minimizes the output power of the linear filter defined in [Van Baelen et al. 1991]. On the other hand, brightness distribution defined in [Chu et al. 1997] could be minimized for each frequency. This would have the solution for the reduction of side lobes which are discussed in the Fourier imaging. We cannot quickly minimize the brightness distribution B($\vec{k}$,f) since one should use null values for the weight vector. The minimization must be constrained such that the frequency response of the weight vector should be unity for the desired direction of $\vec{k}$. This problem can be solved analytically as shown below,

$$min_w B(\vec{k}, f) \quad \text{subject to} \quad e^H w = 1.$$

where,

$$e = \begin{bmatrix} e^{j\vec{k}\cdot D_1} & e^{j\vec{k}\cdot D_2} & \dots & e^{j\vec{k}\cdot D_n} \end{bmatrix}^T \tag{3.10}$$

The brightness distribution is derived by taking inverse of the visibility factor and is given in Equation 3.11 for Capon method. Figure 3.4 shows that for Capon the side lobes were suppressed were as for Fourier beam forming method the interference of side lobes still present.

$$B_c(\vec{k}, f) = \frac{1}{e^H V^{-1} e} \tag{3.11}$$

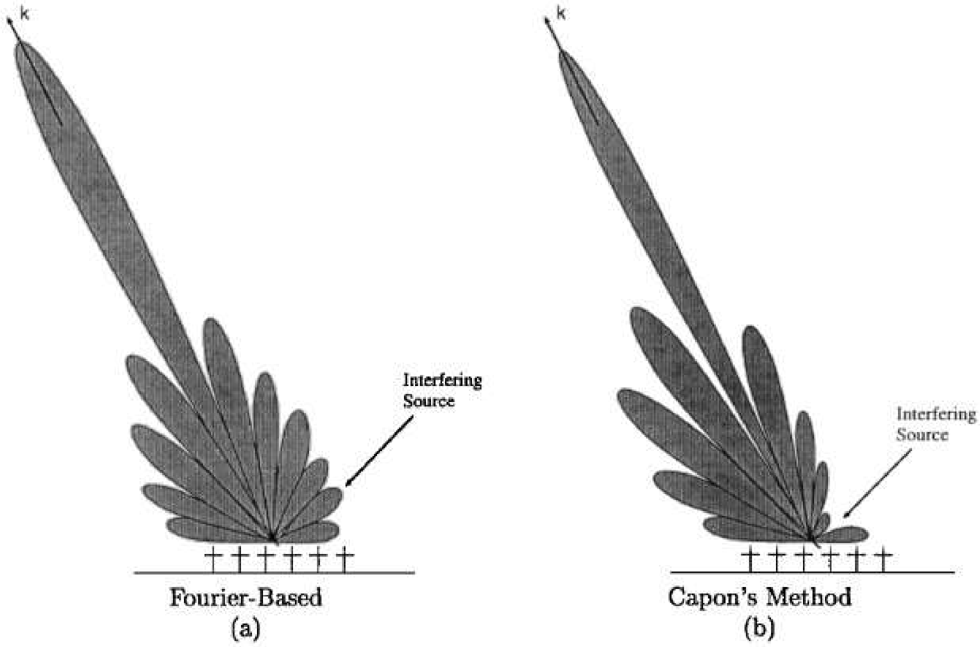

Figure 3.4: The radiation beam pattern for (a) Fourier based imaging, (b) Capon - adaptive beam forming imaging methods [Palmer et al. 1998]

3.4 Maximum entropy

Even after implementing Multiple Input Multiple Output (MIMO) to Capon's method the small structure are not visible clearly and one could get an infinite possible number of solutions for the brightness and the visibility. With all the values, maximum entropy picks the solution with the minimum information content in brightness distribution and most consistent with the visibility data and with some statistical uncertainties [Hysell 1996]. The entropy for the given frequency bin and range can be defined as [Urco et al. 2019]

$$S = \sum B_c(\vec{k}, f) \ln \left[\frac{B_c(\vec{k}, f)}{F} \right] \tag{3.12}$$

$$F = \sum B_c(\vec{k}, f) \tag{3.13}$$

where F is the summation of the brightness distribution over the area of interest. From the solution of Equation 3.8, S is defined as

$$max \text{ (S) is} \left| V - e \cdot B_c(\vec{k}, f) \right| < \epsilon \tag{3.14}$$

where ϵ is the noise amplitude associated with visibility measurement [Urco et al. 2019]. The principle claims that it will lead to a solution with the lower entropy to imply information not contained in data.

Chapter 4

Investigation of PMSE by imaging experiments

The goal of this thesis work is to analyze small scale structure of PMSE for the summer season 2018. By implementing the high-resolution imaging techniques such as Capon and Maximum entropy as well as using Fourier beamforming, for the SIMO and MIMO configurations with MAARSY radar. The overview for the seasonal period for the PMSE starts from the end of the May month. Later it gradually increases in June and July with high intensity. By the mid of August the PMSE and fades out.

4.1 Overview of imaging analysis

From the raw data, we can derive cross-spectra from the recorded voltages (radar echoes). Various imaging methods, Fourier beamforming, Capon's adaptive beamforming and Maximum entropy, are applied to the received voltages from raw data to estimate brightness distribution with the consideration of the radar scattering power as the function of the angle of arrival. The estimated brightness from the imaging will be given in spherical coordinates. To define the spherical coordinates (r, θ, ϕ) [r=radius, θ= inclination, ϕ=azimuth], one must choose zenith and azimuth as reference by considering the origin point in space. This choice determines the reference plane that contains the origin point, which is perpendicular to zenith. The geographic coordinate system uses the azimuth and elevation of the spherical coordinate system (r, θ, ϕ) to express the location on earth called as latitude and longitude. Just like the 2D cartesian coordinate system useful on the plane, 3D spherical coordinate system is useful for the curved surface. This spherical coordinates can be converted to cartesian coordinates with the radar as a centre. After some interpolation we can produce the plots for different x, y, z cuts.

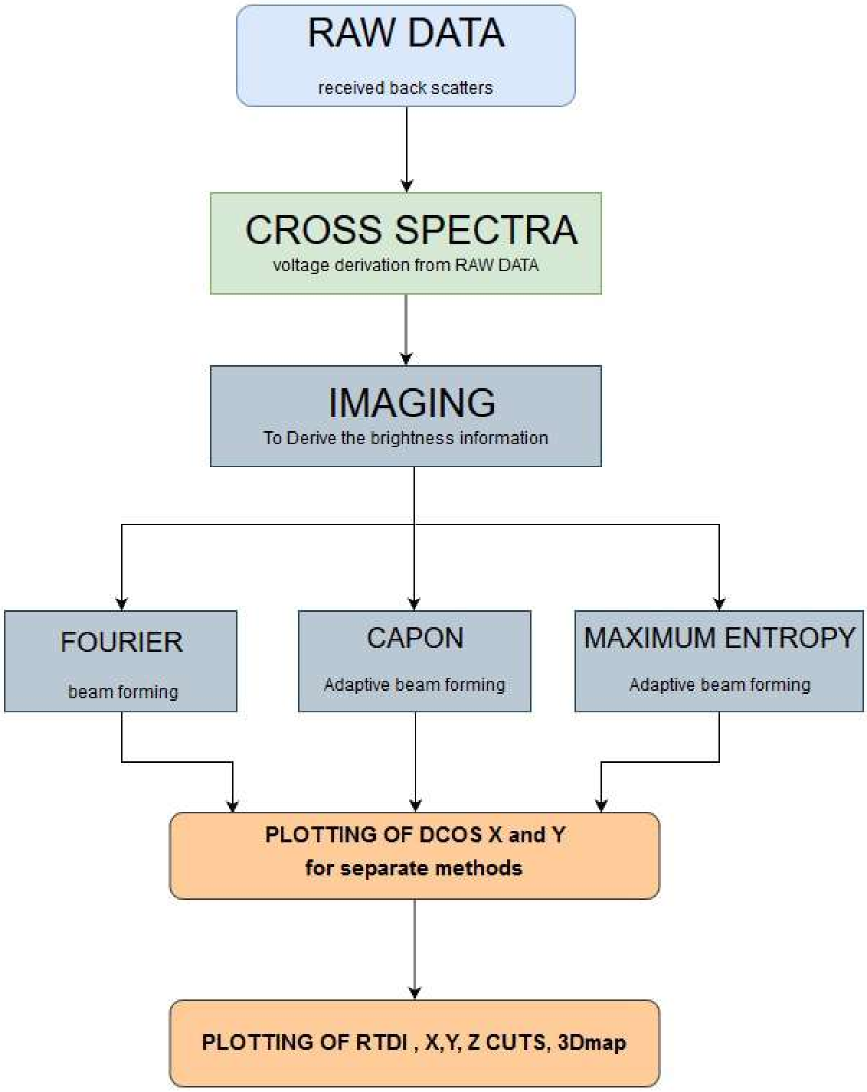

Figure 4.1: Working principle for imaging experiments

The high-resolution imaging generally demands significantly larger computational time than Fourier beamforming methods. Since the resolution of the image produced by the Fourier beamforming is poor, it is computationally inexpensive. Even though Capon produces better resolution images, Maximum Entropy could produce best resolution to resolve the smaller scale structures, but requires respectively large computational time.

4.2 Analysis procedure

4.2.1 Raw data to cross spectra

The information about brightness distribution has been extracted into a cross-spectra as voltages. This spectra will have the coherence of the Doppler frequency (Hz) for each sampled range as well as the phase information for the transmitting and receiving channels. The difference in the quality of the backscatter and the phase information can be seen in Fig. 4.2.

From the raw data, we have to perform several steps to obtain a cross-spectra to proceed with the imaging methods. For instance, removal of DC component i.e. subtraction of the mean of the time series, for phase calibration and storing the voltages (brightness information) as metadata. The total number of ranges and channels list were formulated and data is correlated, concerning the standard UNIX time. With all the known and derived information, the voltages were stored in a matrix format. The transmitter and receivers phases play a significant role in the estimation of brightness information.The calibration of the MAARSY receiver phases is done by the regular observation of cosmic radio source like CassiopeiaA [Chau et al. 2014]. With the wrong phase calculation, we may derive wild structures or blurred structures, with the very strong echoes for each data points due to the phase ambiguity. From the Figure 4.2 Coherence and phase information for two different receiver channels (hexagons) and two transmitters channels are shown with anemones

A-03(Tx), C-03(Rx) and E-03(Tx) , A-03(Rx).

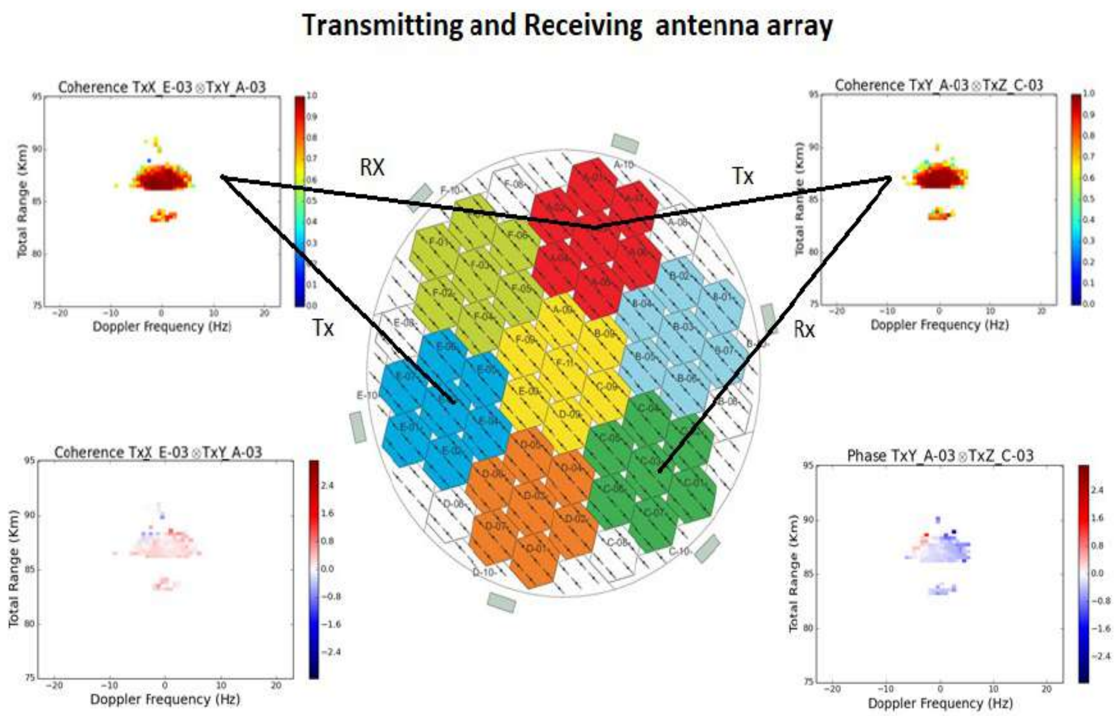

Figure 4.2: Coherence and phase information for two different receiver channels (hexagons) and two transmitters

4.2.2 Applied imaging methods

With the voltage information we perform the different high-resolution imaging techniques such as Capon, Maximum Entropy and Fourier beamforming (inverse fourier transform), which are explained in chapter 3. By implementing three different imaging methods we may estimate the brightness separately for each method, i.e. radar scattering power as a function of angle of arrival. Figure 4.3 shows the distribution of PMSE observed on 8^{th} June 2018 at 13:04:22 using Maximum Entropy method in a MIMO configuration.

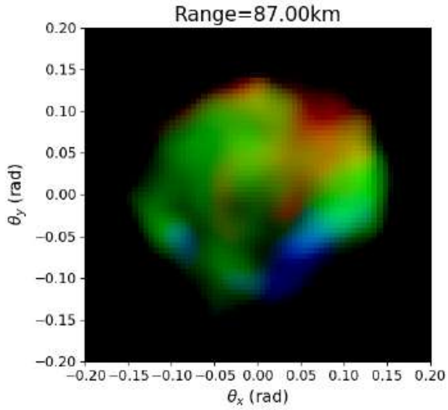

Figure 4.3: Imaging method - Maximum Entropy with MIMO configuration with respect to date and time of 8^{th} June 2018 at 13:04:22.

4.2.3 Plotting for coordinate axis cuts

Since the estimated brightness is expressed in polar coordinates (θ_x, θ_y, r), we apply the cube spline interpolation to convert them in to Cartesian coordinates, B(θ_x, θ_y, r) to B(x, y, z), considering the radar located at center(x=0, y=0, z=0). Finally we plot for the Range Time Doppler Intensity (RTDI) and for the selected cuts x and y vs. the altitudes and z cut vs North-South and East-West direction.

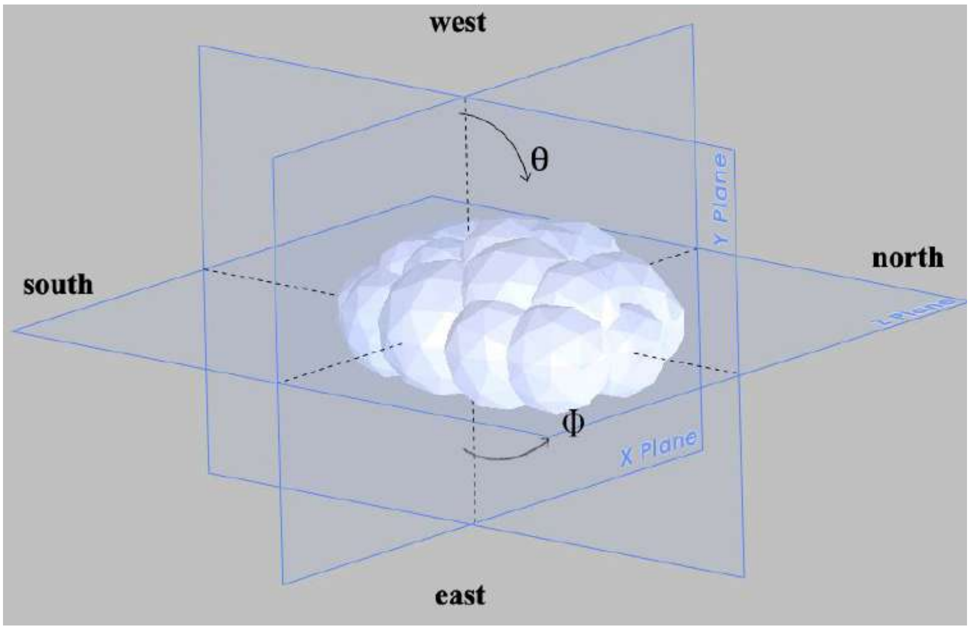

Figure 4.4: x, y and z plane cuts corresponding to the direction north-south and east-west aligned to the radar

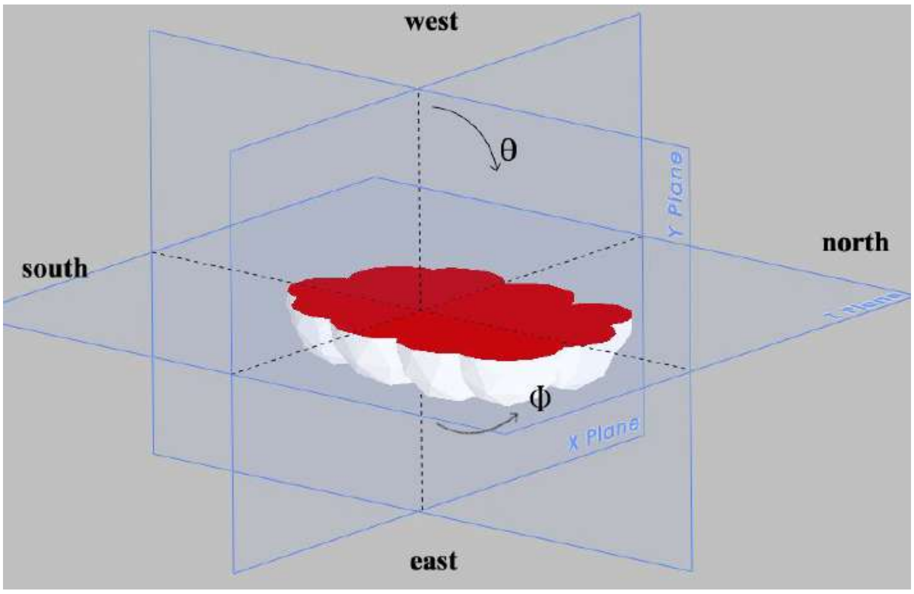

Figure 4.5: zcut for the north-south and east-west direction

Figure 4.5 is the synthetic reference of zcut of Figure 4.6 shows the horizontal cut for the north-south and east-west direction corresponding the the altitude of 86 km. From figure, we can analyze the structure of the PMSE and direction of the wind flow.

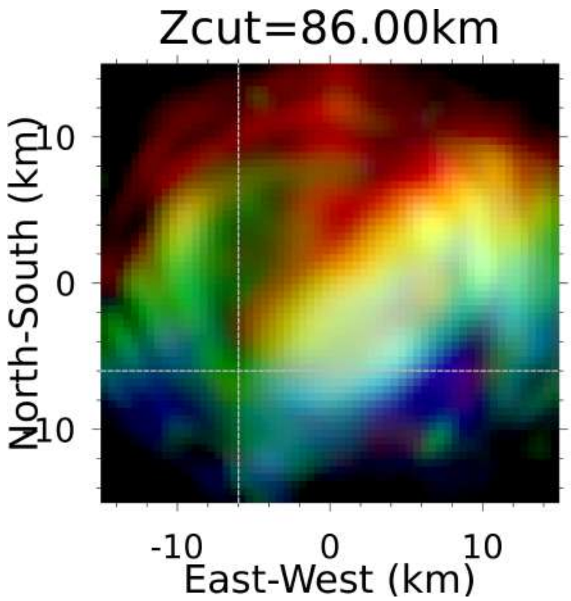

Figure 4.6: Maximum Entropy MIMO event 2, zcut= 86 km for the north-south and east-west direction

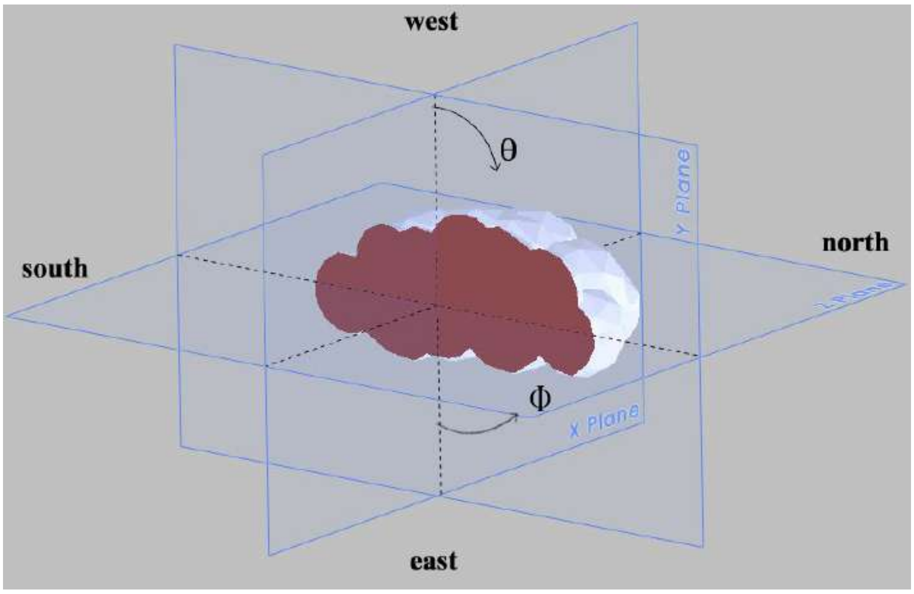

Figure 4.7: Vertical plane cut for the altitude vs. ycut

Figure 4.8 shows the vertical plane cut for the altitude vs. ycut= 6.00 km, with the range of +/- 10 km direction. From figure, we can analyze the wave structure of the PMSE, direction of the wind flow from meridional direction for the different altitudes.

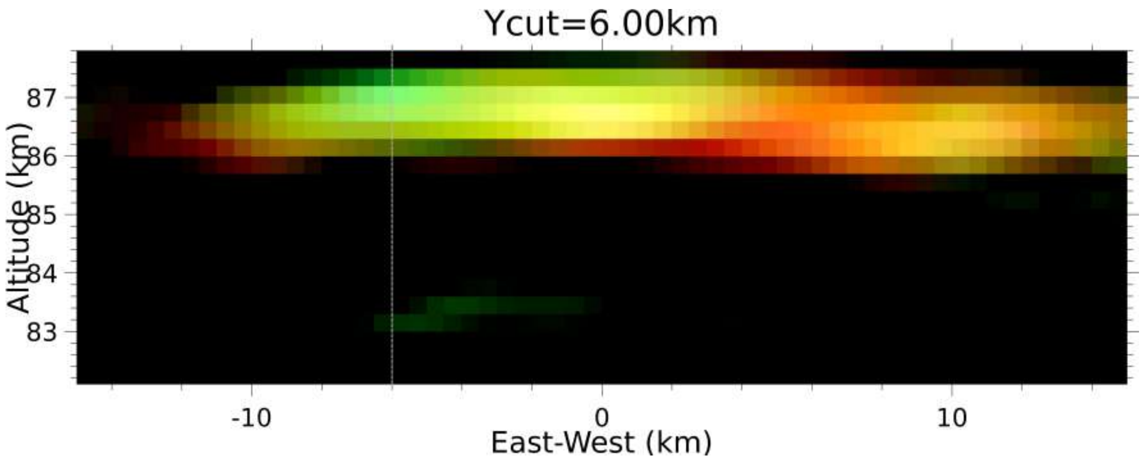

Figure 4.8: Maximum Entropy MIMO event 2, zcut= 86 km, y= 6 km for the north-south vs. altitude

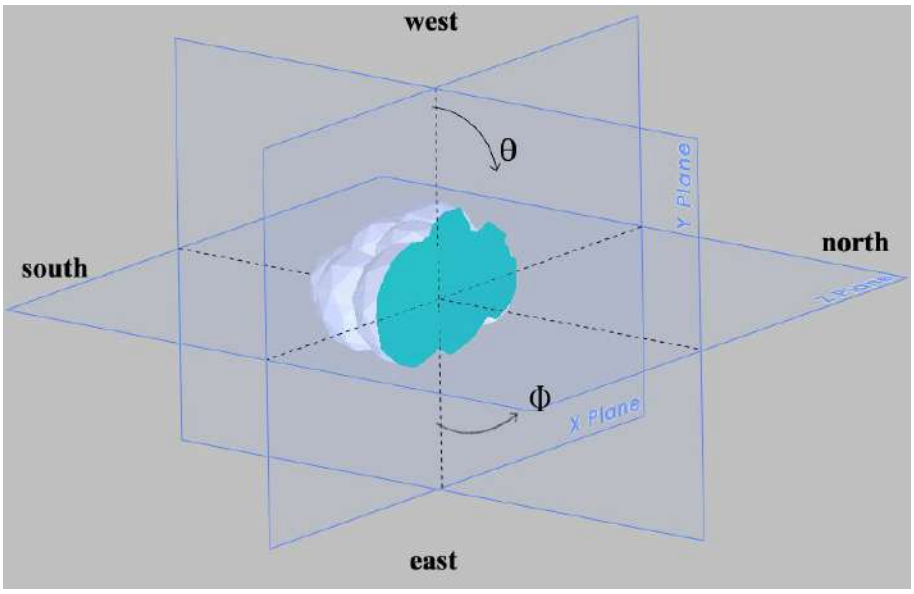

Figure 4.9: Vertical plane cut for the altitude vs. xcut

Figure 4.10 shows the vertical plane cut for the altitude vs. xcut= -4.00 km, with the range of +/- 10 km direction. From this Figure 4.10 we can analyze the wave structure of the PMSE and the direction of the wind flow from zonal direction for the different altitudes.

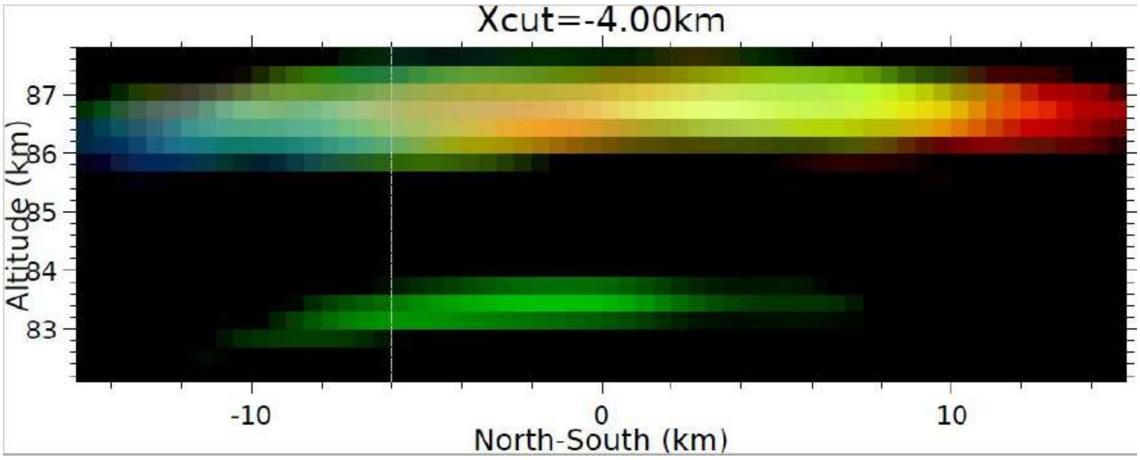

Figure 4.10: Maximum Entropy MIMO event 2, zcut= 86 km, x= -4 km for the north-south and altitude

Chapter 5

Result and Discussion

5.1 Result

Figure 5.1 shows the resulting Range Time Doppler Intensity (RTDI) in vertical beam for the single example on 2018 June from 13:00 to 14:00 UT. This plot is obtained from Maximum Entropy for MIMO configuration of the back scatters signal for various altitudes with appropriate universal time. Combining the SNR and Doppler information we get the RTDI plot. The signal intensity is represented as lightness, Doppler information as hue and spectral width as saturation. In this work only for 2 events data are analyzed in detail, but looking to many days of data with large SNR. The chosen two examples to focus on the observed structures and their apparent motion. The entire list of the analyzed data can be found in **??** and Table 3.

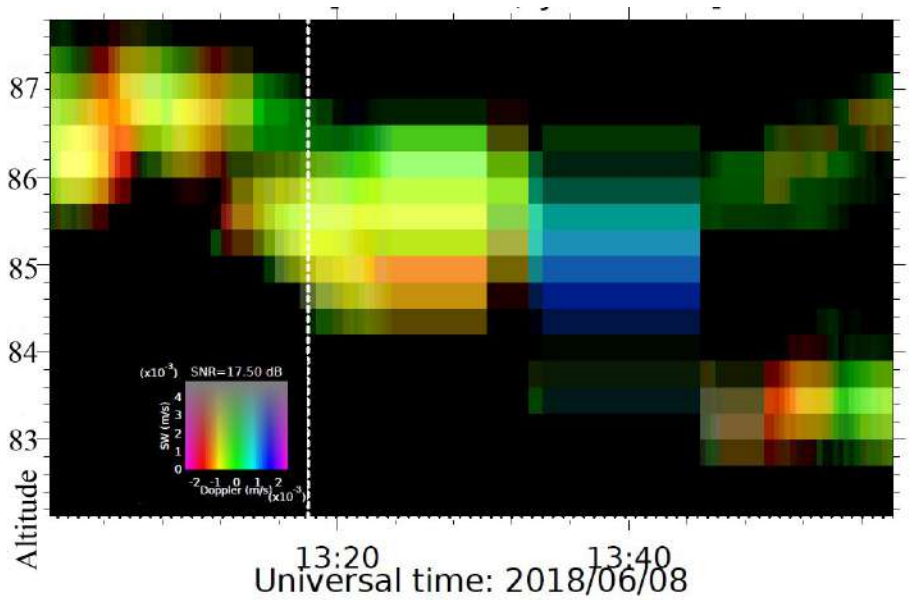

Figure 5.1: The Range Time Doppler Intensity (RTDI) plot of PMSE using MIMO Maximum Entropy for time vs. altitude in km

5.1.1 SIMO vs. MIMO of imaging methods

From the imaging method we derive the brightness information in spherical coordinates B(θ_x, θ_y , r), which has to be converted in to Cartesian coordinates B(x, y, z) by implementing a cube spline interpolation to analyze different plane cuts by considering the radar location as center (x=0, y=0, z=0). Figure 5.2 shows the comparison of SIMO and MIMO to understand different imaging methods. Also, the x vs. y cuts for the given z, as well as x vs. z for the given y and y vs. z for the given x represents the East-West (EW) direction, North-South (NS) and the altitude respectively. The corresponding red, green and blue colour represents the Doppler shift, red is strong positive Doppler, blue is negative Doppler and the green is zero Doppler shift.

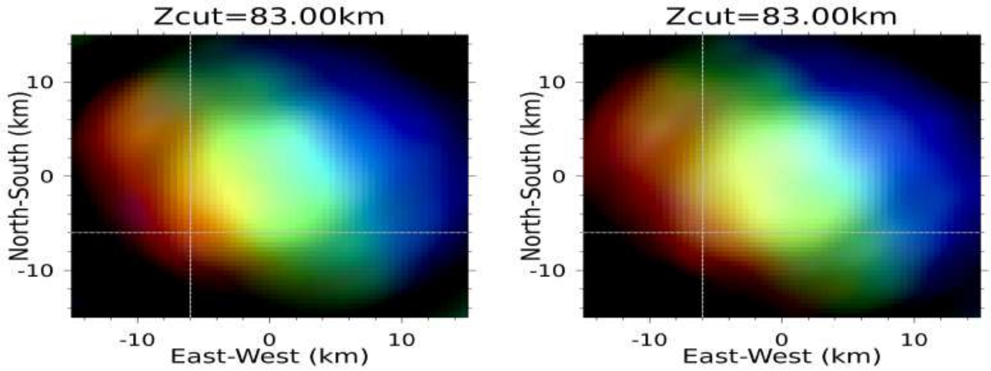

(a) SIMO Capon event 1

(b) MIMO Capon event 1

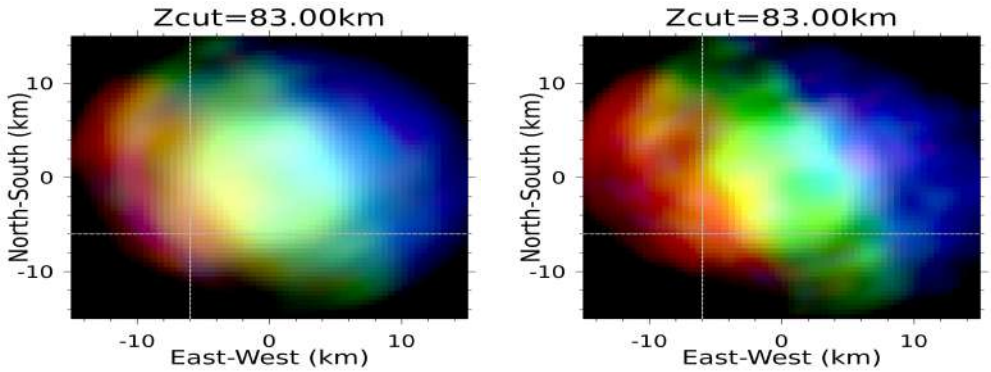

(c) SIMO Maximum Entropy event 1

(d) MIMO Maximum Entropy event 1

Figure 5.2: Comparison of SIMO vs MIMO for Capon and Maximum Entropy at 07:19:06 UT on 19th June 2018, i.e. event 1. The horizontal and vertical dotted lines represents the location of the NS-EW cuts

For the comparison of MIMO and SIMO, we choose two separate events from summer 2018. Figure 5.2 is the choice of event 1 on 2018 June 19th at 07:19:06 UT to study the multiple layers of PMSE. From the MIMO we achieve a clear and well-defined image compared to the SIMO results. MIMO Capon method further improves the quality by making the small scale structural variations visible and can be seen in Figure 5.2 (b). A further improvement is visible employing the Maximum Entropy method, resulting in an even better resolution of the fine structures as can be seen in Figure 5.2 (d).

Due to the larger virtual antenna array, MIMO shows nearly 50% improvement over SIMO configuration for both Capon and Maximum entropy. Maximum entropy qualitatively outperforms the Capon. On the other hand, Capon tries to reduce the side lobes by wisely choosing the antenna weight to perform the echo-free zone. Capon performs better than conventional beamforming (Inverse Fourier Transform).

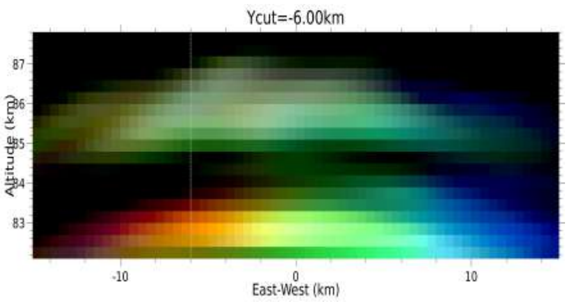

(a) SIMO Capon event 1

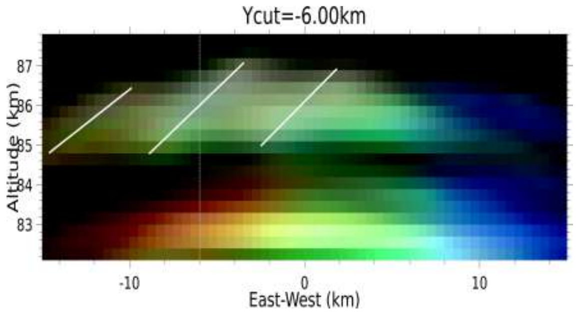

(b) MIMO Capon Event 1

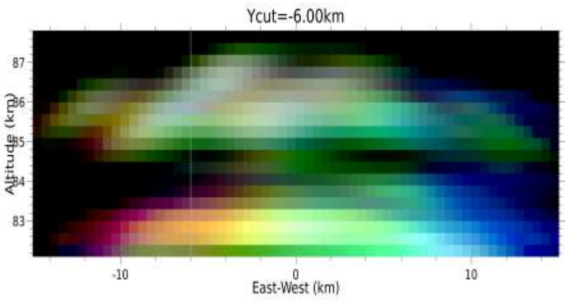

(c) SIMO Maximum Entropy event 1

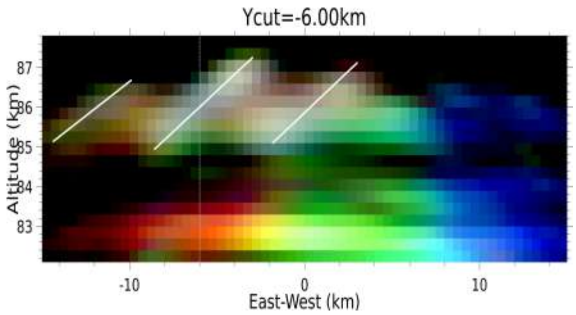

(d) MIMO Maximum Entropy event 1

Figure 5.3: Comparison of SIMO vs MIMO for Capon and Maximum Entropy at 07:19:06 UT on 19^{th} June 2018, i.e. event 1 represents EW - Altitude cut at Ycut= -6 km. The white line indicates the waves with respect to direction

Coming back to the comparison of SIMO and MIMO results of Capon and Maximum Entropy. The Figure 5.3 for ycut= -6.00 km vs. altitude is an effective example to study the different horizontal layers of PMSE . The red, blue and green represents the Doppler shift. The red color represents the wave coming towards us, blue color represents the wave moves away and green color represent the zero movement of wave. MIMO CAPON and MIMO Maximum Entropy show the well-defined structure of the two different layers of the PMSE.

The following parameters of the observed structure can be summarized as follows:

- A wave-like structure between 85 km to 87 km with a horizontal wavelength of approximately 3.5 km.
- A nominal structure of between 82 to 84 km. Similarly, we can see a different structure in event 2. at 13:04:22 on 8^{th} June 2018.
- The wave structure propagates towards the west direction and can be seen in the ycut with a wave-like structure with the wavelength of approximately 10 km.

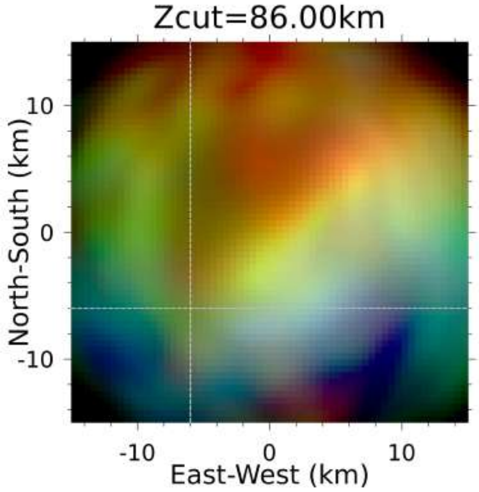

(a) SIMO Capon event 2

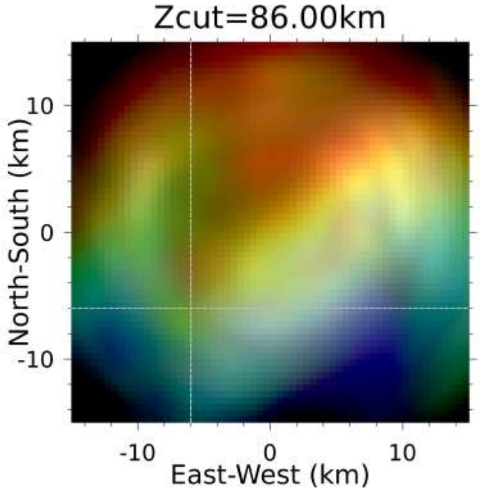

(b) MIMO Capon event 2

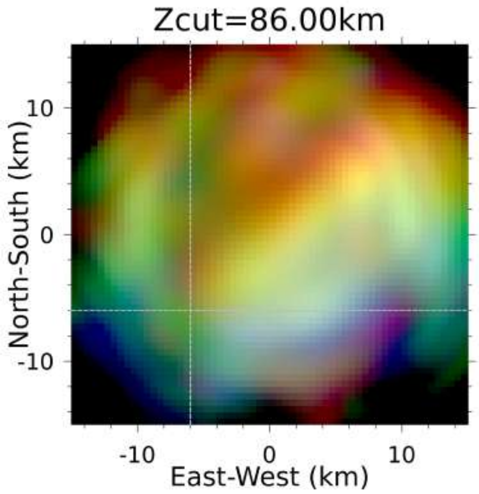

(c) SIMO Maximum Entropy event 2

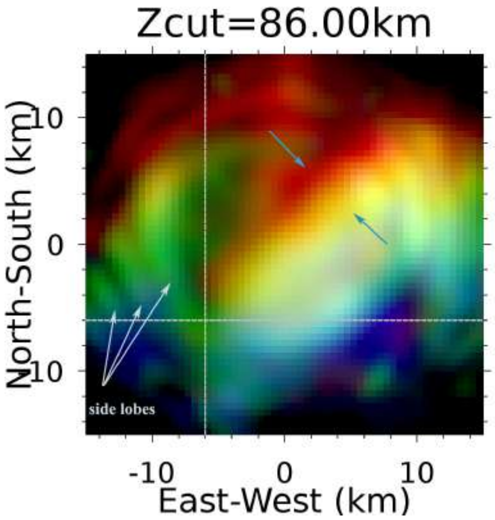

(d) MIMO Maximum Entropy event 2

Figure 5.4: Comparison of SIMO vs MIMO for Capon and Maximum Entropy at 13:04:22 on 8^{th} June 2018, i.e. event 2. The horizontal and vertical dotted lines represents the location of the NS-EW cuts

The Figure 5.4 shown the event 2 at 13:04:22 on 8^{th} June 2018. similarly to event 1 the MIMO outperforms the SIMO configuration about 50% in quality. Also observe the concentric ring structures around the wave structure. These concentric rings arise due to the superposition of the receiving channels (receiving hexagons)with the transmitter pattern approximately 5.5°. The superposition leads the transmit pattern moves slightly up to + 8 km or - 8 km. The sample Figure 4 and Figure 5 are given in section C .

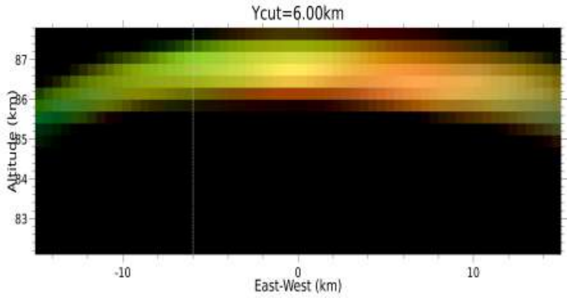

(a) SIMO Capon event 2

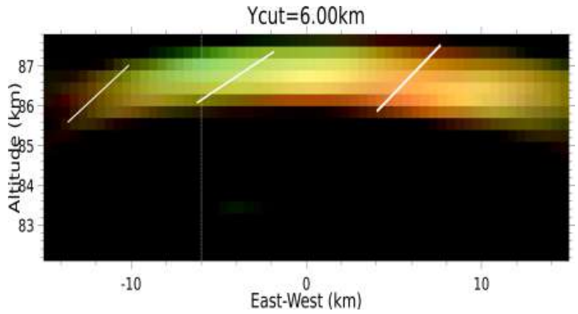

(b) MIMO Capon event2

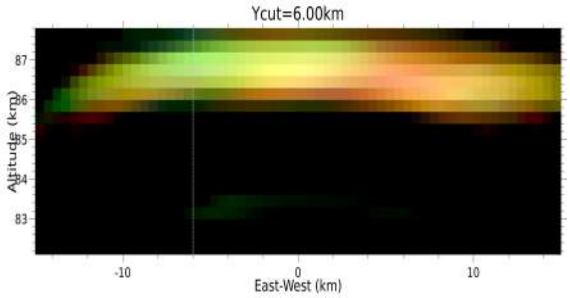

(c) SIMO Maximum Entropy event2

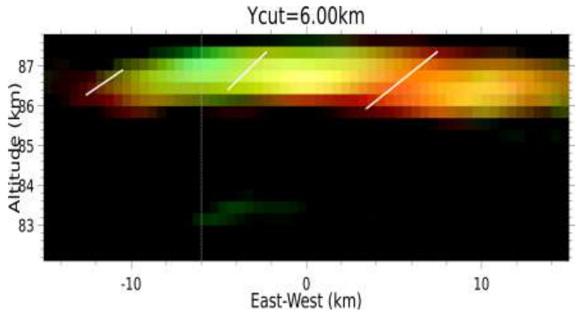

(d) MIMO Maximum Entropy event2

Figure 5.5: Comparison of SIMO vs MIMO for Capon and Maximum Entropy at 13:04:22 on 8^{th} June 2018, i.e. event 2. East-West altitudinal cut at Ycut= -6 km

Figure 5.5.d gives us an interesting structure that the wave doesn't maintain a constant amplitude in vertical direction, instead it gradually increases and fades out. The wave structure is elongated in the zonal direction. the direction of the wind flows form the north west to south east direction.

5.1.2 MIMO results 2018

The MIMO results of the Maximum Entropy are taken and discussed for the event 2. shows echo power and doppler information of the time evaluation vs. altitude for the selected East-West and north-south direction. Form theses plots we can analyze how the horizontal structure of PMSE evolves with time for the different altitudes.

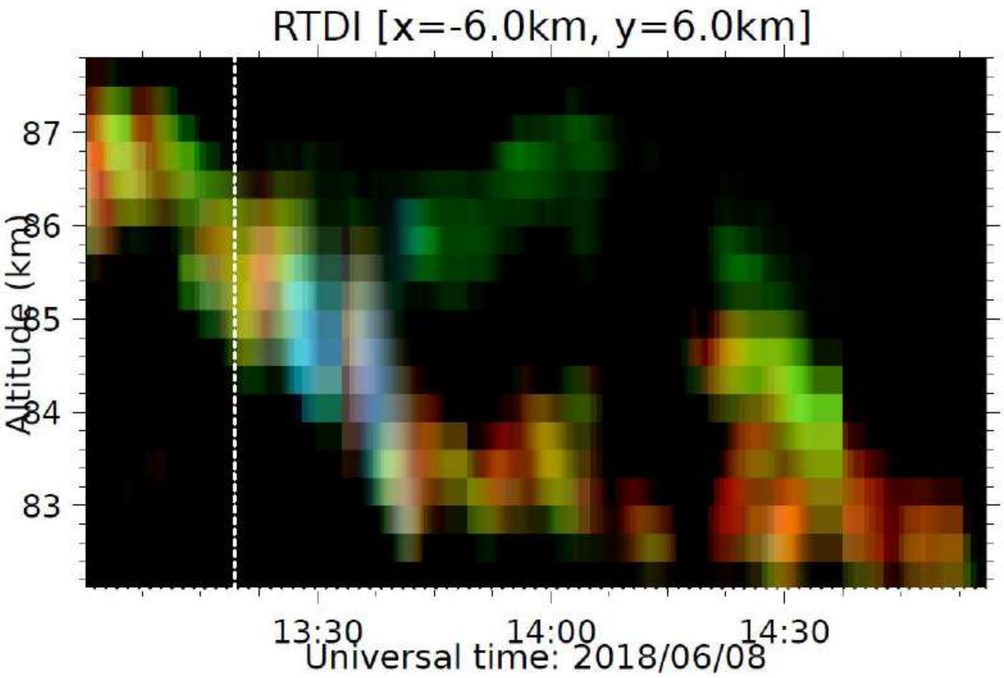

Figure 5.6: Maximum Entropy MIMO; Range Time Doppler Intensity (RTDI) for the PMSE structure as the function of altitude and time for event 2

Figure 5.6 shows the event 2 at x = -6 *km*, y = 6 *km* and gives an overview of the difference in the intensity of backscatter for different altitudes over time. The dotted white line represents the vertical range cuts for the time around 13:23:55 UTC.

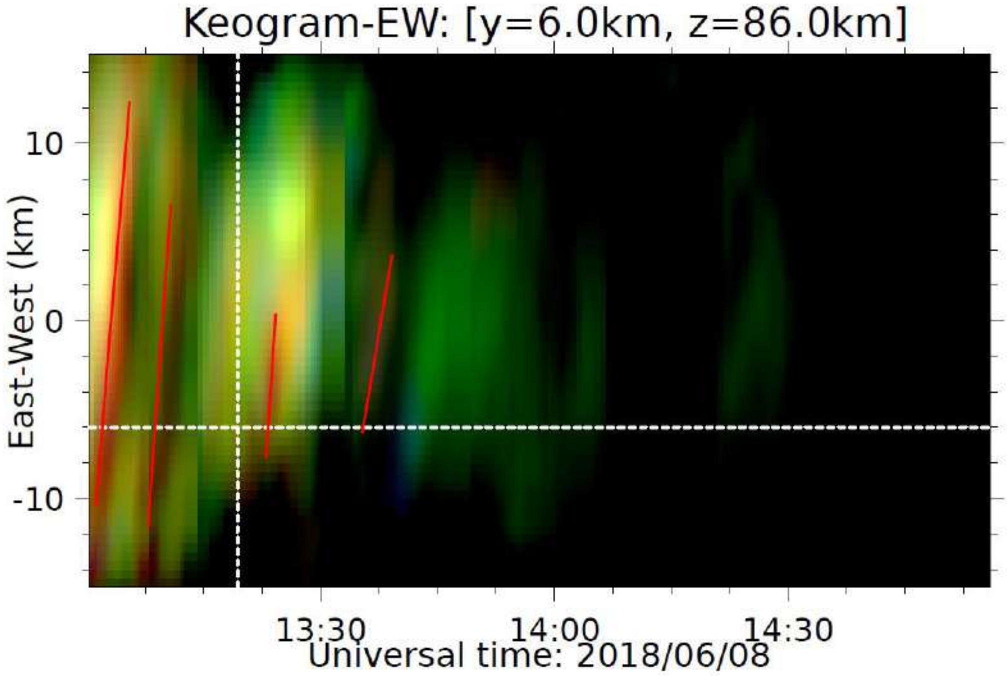

Figure 5.7: Keogram image of the PMSE structure as the function of time vs EW location plot for the event 2 on 8^{th} June 2018

Figure 5.8 and Figure 5.7 represent the time evaluation direction for NS and EW keogram respectively. The keogram event 2 between 13:00:00 and 15:00:00 on 8^{th} June 2018 with a total power of 17 dB shows the meridional oriented wave is limited up to 86 km and the wave propagates in zonal direction. In Figure 5.7 we see that the wave propagates against the wind direction and descends in altitude over time, so we see the red lines shrink and disappear. But in the Figure 5.8 we see the negative Doppler in meridional direction and the waves traveling in the zonal direction. Hence it proves that the wind estimation from the RTDI can be verified with the keograms for the better understanding of the wave structure and its motions.

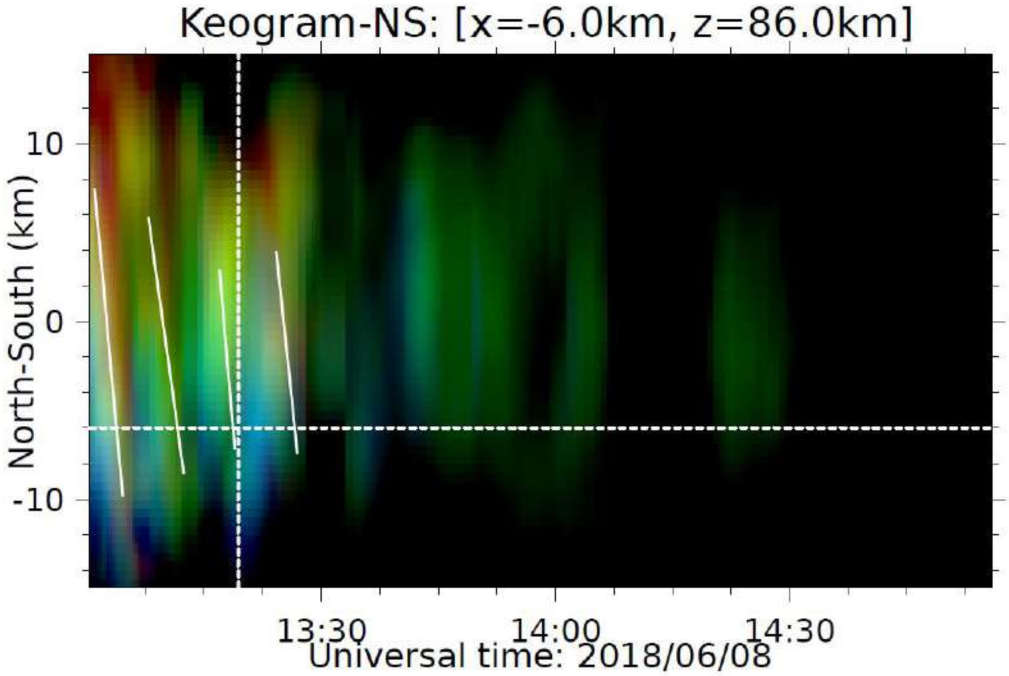

Figure 5.8: Keogram image of the PMSE structure as the function of time vs. north-south location plot for the event 2 on 8^{th} June 2018

In the north-south direction, the meridional wave is drifted and was not observed clearly but the drift is visible in zonal direction. The Mesospheric waves like structure are drifted and moves along with the background wind. These fluctuations have been correlated with breaking down of the gravity wave, this shows the clear representation of instability in the atmosphere [Chau et al. 2019].

5.2 Discussion

The detail discussion of a special event from Figure 5.9 is the choice to analysis the two distinct layer of horizontal structure of PMSE. At lower altitude we see the strong backscattering with no influence on the vertical motion of the wave structure. The observed structure appear to move along with the background wind. On the other side, at a higher altitude we can see the curly wave motion with the vertical movement of up-welling and down-welling .

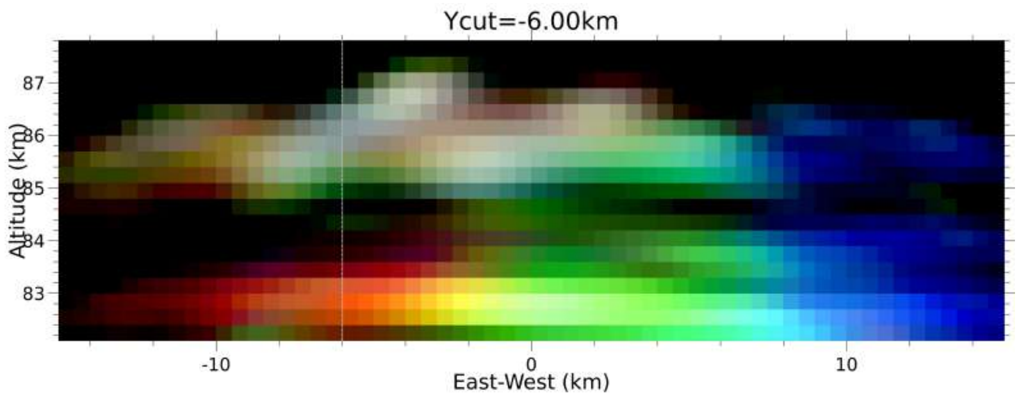

Figure 5.9: Maximum Entropy MIMO for Y cuts at 13:04:22 on 8^{th} June 2018, i.e. event 1. Show the two different layers and its variation in vertical motion of wind in a curly wave motion

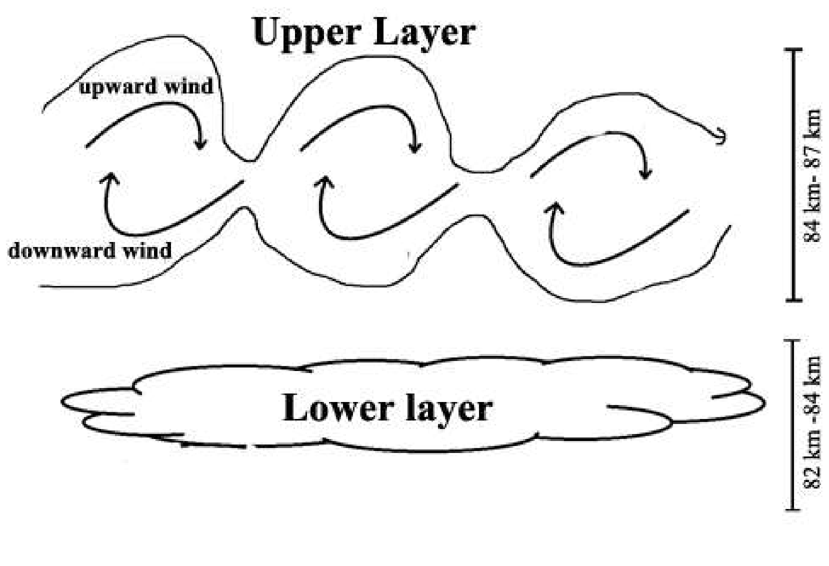

Figure 5.10: The horizontal motion of the wind in Up and down welling for upper layer to the event 1 on 8^{th} June 2018

This vertical motion of the wave might be a cause of turbulence and it can be seen in Figure 5.10. The motion of wave structure has the different wind velocity for the upward wind and downward wind and at center the wind speed will be same as the wave. This curly motion descends in altitude over time and could diffuse to the lower layer. This leads a necessity to the analysis of the instability, also known as the Kelvin–Helmholtz instability. The Kelvin–Helmholtz instability (KHI) may results from the turbulence of the two air layers close to each other which moves in different speed and direction also called as wind shear [Chau et al. 2019; Stober et al. 2018] .

5.2.1 Comparison of DBS with imaging

The Comparison of DBS and imaging is used to analyze the direction of the wave like structure (PMSE) moves along with the wind are observed and seen in Figure 5.11. From the result of Maximum Entropy MIMO at 13:04:22 on 8^{th} June 2018 for the altitude of 86 km, we can see a strong wind flow from the north towards the south-west direction. Comparing the apparent movement of the PMSE as seen with imaging MIMO with the Doppler Beam Swinging results as shown in Figure 5.11, the measurements of the north pointing DBS beam shows a positive radial velocity , which agrees to the negative radial velocity in the south beam. Moreover from the east side, there might be a drift in wind direction with very low radial velocity slightly above zero. This conforms the wind direction moves from the north towards the south-west. From 13:12 UT on the PMSE layer descends from 86-88km to approximately 84-86 km altitude can be seen in Figure 5.11 (a).

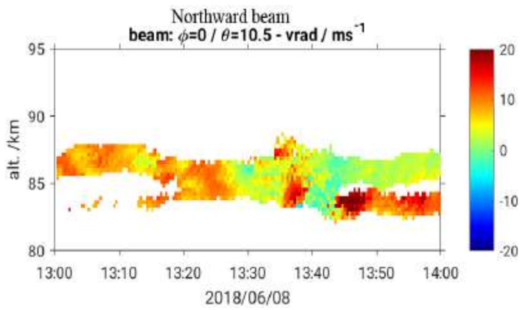

(a) Northward beam-DBS

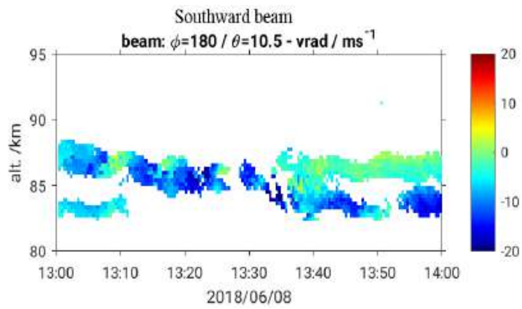

(b) Southward beam-DBS

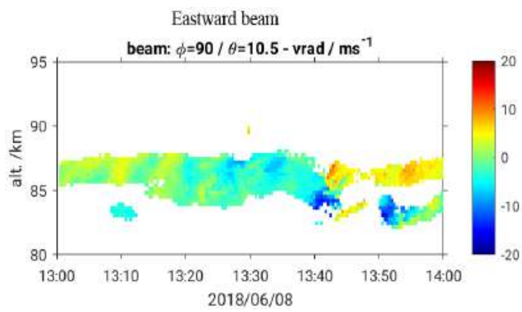

(c) Eastward beam-DBS

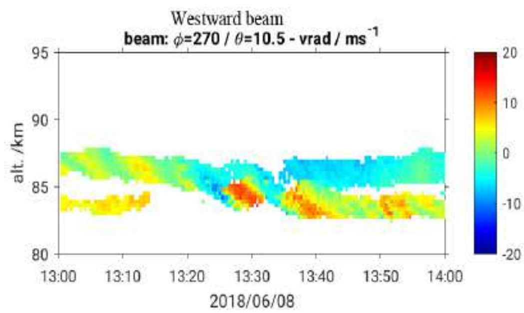

(d) Westward beam-DBS

Figure 5.11: DBS - radial velocity for the different direction

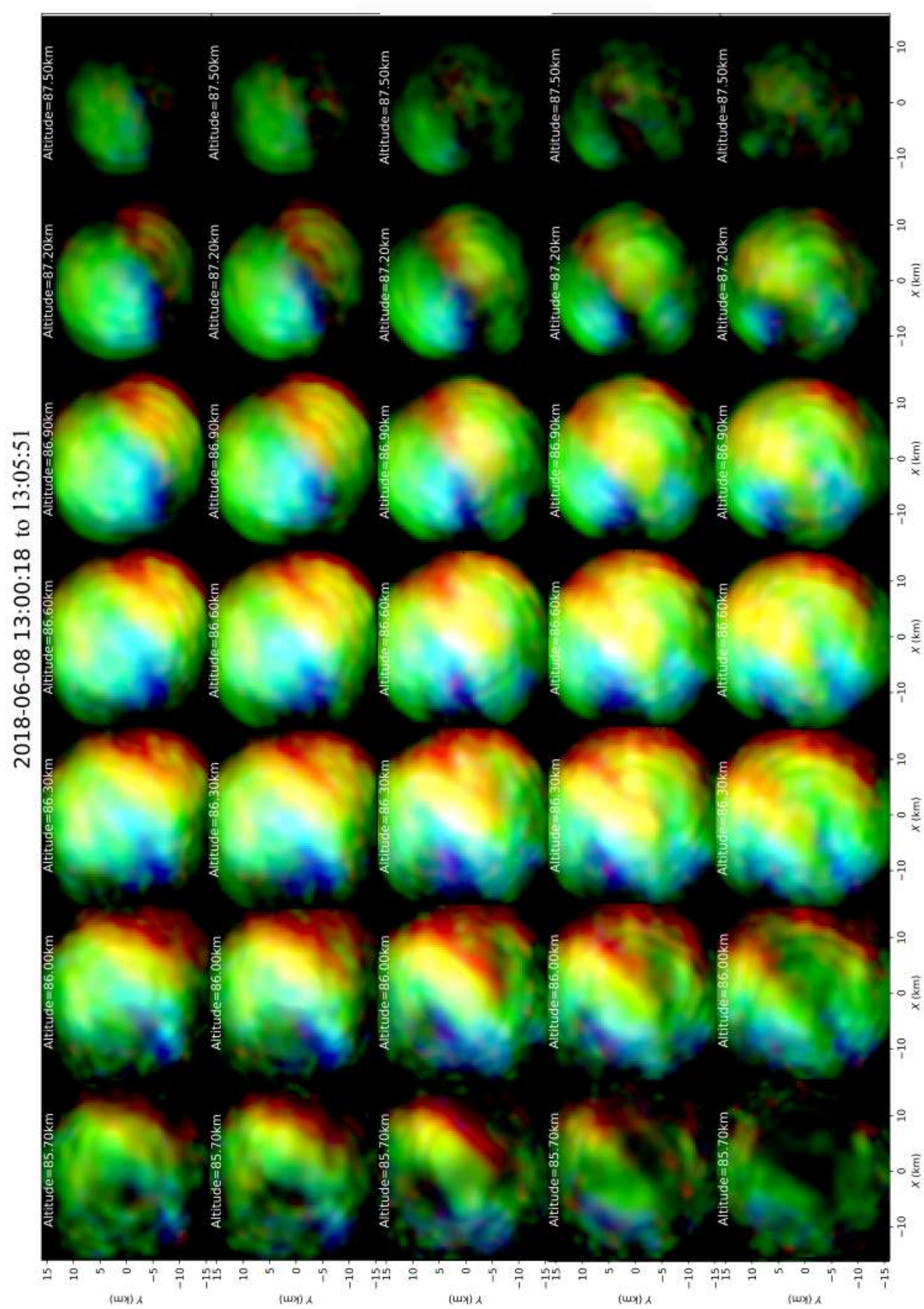

Figure 5.12: The altitude variation in the wind direction from 85 km to 87.5 km are observed on 8^{th} of June 2018 from 13:00:18 to 13:05:51 UT

From the Figure 5.13 is a result of imaging (Maximum Entropy MIMO) for the horizontal zcuts = 86 km for north south and east west direction is taken to view the motion of wave like structure. The movement of wave in north-west direction which can be clearly seen by marking of yellow line on the white spot. For different altitudes the imaging gives us the better quality image for wind profilers. For example

Figure 5.12 at 86 km the evaluation of the wave and its direction of flow are more clear than the upper and lower altitude .

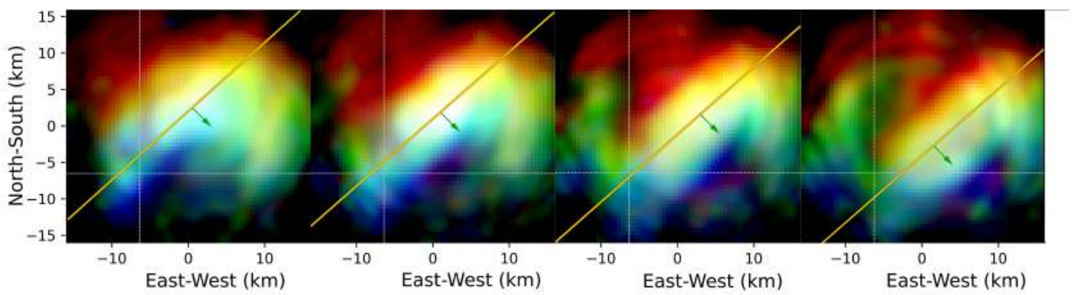

Figure 5.13: At 86 km Altitude for the different time steps of one minute interval on 8^{th} of June 2018 from 13:00:18 to 13:05:51 UT. The movement of the wind were shown in the yellow line and green arrow indicates the direction of flow

The movement of wind direction in the horizontal cut at zcut = 86 km to the corresponding north-south and east-west direction for a few minutes were studied. This shows the movement of wind travels with rise and fall for a particular region with respect to time. The motion of the wave structure elongated north-west direction and travels along with the wind. The the rise and fall of the amplitude of the wave structure is visible y plane. This variation is clearly spotted in the Figure 5.14 blue spot near the yellow line.

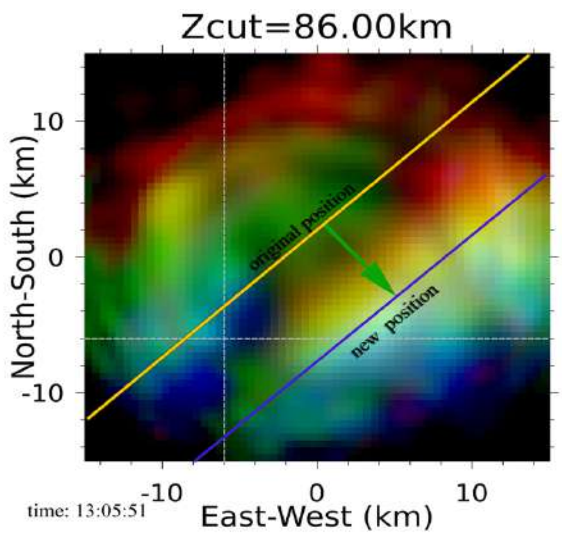

Figure 5.14: At 86 km altitude for the time interval of 5 minute transition. The structure are moved by the wind are shown in the yellow line (initial position), blue line (final position) and green arrow indicates the direction of the flow

5.2.2 Aspect sensitivity of PMSE structure

We choose the event 2 to verify the motion of small scale structure of PMSE from the keograms. We have seen in Figure 5.7 that the wave was drifted along with the wind direction, where the scatterer travel in the opposite direction. Over some time, we see that the scatterer curling with the path of the wind .

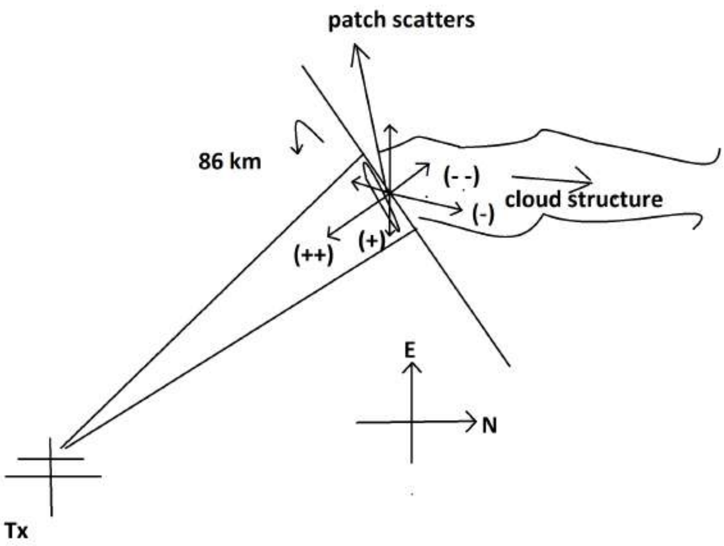

Figure 5.15: Aspect sensitivity of the patchy scatterer in the horizontal structure of PMSE movement at 86 km for the event 2

From Figure 5.15, we can determine the motion of the scatterer at 86km is not a constant horizontal surface. The patchy scatterer curls in all direction , when the scatterer moves against the radar the scattering is too strong and low in the opposite direction i.e. indicated in Figure 5.15 with (++) and (–) values results in irregular scattering. the horizontal structure of PMSE are not aligned in isotropic manner and moves in dynamic behaviour. in conclusion the PMSE was not totally depended on the aspect sensitivity instead it widely depends on the background wind, turbulence, layering of charged ice particles. This gives us a new area to work further. (1) reduction layer thickness over a period of time. (2) will be that tracking of the small patches with the multiple layers of PMSE. (3) is the analysis of the KHI instability.

Chapter 6

Conclusion

In this thesis work, the successful implementation of the coherent radar imaging with the MAARSY Radar for SIMO and MIMO configuration has been done to observe the Polar Mesospheric Summer Echoes. The obtained results for SIMO and MIMO for the different imaging methods were investigated with quality of resolution for Capon and Maximum Entropy. applying the MIMO configuration a larger virtual antenna array is obtained. With this enlarged antenna array size and hence the resolution has been improved significantly.

Applying Maximum Entropy for the MIMO configuration gives the best resolution enabling us to see structures with less than 3.5 km. The movie is included with the optical disc, it shows the wave motion of the PMSE structure. The horizontal structural analysis of PMSE shows the wave length of 2.5 in east-west direction with an inclination and the wave structure is elongated in the order of 8 km in north-west for the event 2. The comparison of DBS with the imaging gives visual analysis of the wave like structure moved along with the wind and the direction of wave flow is visible for each time intervals.

The aspect sensitivity of the horizontal structure of PMSE were discussed. The patchy scatterer moves in all direction with respect to time and its not constant in nature, so the horizontal structure will not be in aligned horizontally. This results that the occurrence of PMSE is not due to the aspect sensitivity, but might be the cause of turbulence, background wind and other dynamics of atmosphere.

We have shown the quality of the radar imaging of the PMSE is significantly improved by using MIMO over SIMO configuration. It show significant improvement for MIMO over SIMO. The comparison of DBS with the imaging are done to estimate the direction of wind flow with the help of horizontal zcuts for x vs. y cuts at different altitude ranges separately. This horizontal cut helps to track the motion of the small scale structures of PMSE in a certain period of time. The results of event 2 show the aspect sensitivity is not the source for the PMSE. Given the computational costs (see subsection B.2), for real time analysis Capon can be used. While for special events Maximum Entropy can be used to improve the resolution on the expense of significantly increased computational time.

References

Doppler Beam Swinging, 2013. URL `http://cfa.aquila.infn.it/wiki.eg-climet.org/index.php5/Doppler_beam_swinging_(DBS)`.

B. Balsley, W. Ecklund, and D. Fritts. Vhf echoes from the high-latitude mesosphere and lower thermosphere: Observations and interpretations. *Journal of The Atmospheric Sciences - J ATMOS SCI*, 40:2451–2466, 10 1983. doi: 10.1175/1520-0469(1983)040<2451:VEFTHL>2.0.CO;2.

E. Becker and S. L. Vadas. Secondary gravity waves in the winter mesosphere: Results from a high-resolution global circulation model. *Journal of Geophysical Research: Atmospheres*, 123(5):2605–2627, 2018. doi: 10.1002/2017JD027460. URL `https://agupubs.onlinelibrary.wiley.com/doi/abs/10.1002/2017JD027460`.

J. Capon. High-resolution frequency-wavenumber spectrum analysis. *Proceedings of the IEEE*, 57(8):1408–1418, Aug 1969. doi: 10.1109/PROC.1969.7278.

J. Chau, J. Urco, V. Avsarkisov, J. Vierinen, R. Latteck, C. Hall, and M. Tsutsumi. Four dimensional quantification of kelvin-helmholtz instabilities in the polar summer mesosphere using volumetric radar imaging. *Geophysical Research Letters*, n/a(n/a), 2019. doi: 10.1029/2019GL086081. URL `https://agupubs.onlinelibrary.wiley.com/doi/abs/10.1029/2019GL086081`.

J. L. Chau, T. Renkwitz, G. Stober, and R. Latteck. Maarsy multiple receiver phase calibration using radio sources. *Journal of Atmospheric and Solar-Terrestrial Physics*, 118:55 – 63, 2014. ISSN 1364-6826. doi: https://doi.org/10.1016/

j.jastp.2013.04.004. URL http://www.sciencedirect.com/science/article/pii/S136468261300117X. Recent progress from networked studies based around MST radar.

Y.-H. Chu, T.-Y. Chen, and T.-H. Lin. An examination of the wind-driven effect on the drift of precipitation particles using the Chung Li VHF radar. *Radio Science*, 32(3):957–966, 1997. doi: 10.1029/97RS00057. URL https://agupubs.onlinelibrary.wiley.com/doi/abs/10.1029/97RS00057.

M. J. Fitch and R. Osiander. Terahertz waves for communications and sensing. 2004.

S. Fukao, T. Sato, R. M. Harper, and S. Kato. Radio wave scattering from the tropical mesosphere observed with the jicamarca radar. *Radio Science*, 15(2):447–457, 1980. doi: 10.1029/RS015i002p00447. URL https://agupubs.onlinelibrary.wiley.com/doi/abs/10.1029/RS015i002p00447.

W. K. Hocking, J. Röttger, R. D. Palmer, T. Sato, and P. B. Chilson. *Atmospheric Radar: Application and Science of MST Radars in the Earth's Mesosphere, Stratosphere, Troposphere, and Weakly Ionized Regions*. Cambridge University Press, 2016a. doi: 10.1017/9781316556115.

W. K. Hocking, J. Röttger, R. D. Palmer, T. Sato, and P. B. Chilson. *Atmospheric Radar: Application and Science of MST Radars in the Earth's Mesosphere, Stratosphere, Troposphere, and Weakly Ionized Regions*. Cambridge University Press, 2016b. doi: 10.1017/9781316556115.

P. Hoffmann, M. Rapp, R. Latteck, A. Serafimovich, and W. Singer. Multiple layer PMSE structures: statistical results from six years of PMSE observations and possible physical explanations of their observed properties. In B. Warmbein, editor, *European Rocket and Balloon Programmes and Related Research*, volume 530 of *ESA Special Publication*, pages 315–320, Aug 2003.

D. L. Hysell. Radar imaging of equatorial F region irregularities with Maximum Entropy interferometry. *Radio Science*, 31(6):1567–1578, 1996. doi:

10.1029/96RS02334. URL https://agupubs.onlinelibrary.wiley.com/doi/abs/10.1029/96RS02334.

D. H. Johnson and D. E. Dudgeon. *Array signal processing : Concepts and Techniques / Don H. Johnson, Dan E. Dudgeon*. P T R Prentice Hall Englewood Cliffs, NJ. ISBN 0130485136.

E. Kudeki and F. Sürücü. Radar interferometric imaging of field-aligned plasma irregularities in the equatorial electrojet. *Geophysical Research Letters*, 18(1): 41–44, 1991. doi: 10.1029/90GL02603. URL https://agupubs.onlinelibrary.wiley.com/doi/abs/10.1029/90GL02603.

R. Latteck, W. Singer, M. Rapp, B. Vandepeer, T. Renkwitz, M. Zecha, and G. Stober. MAARSY-The new MST radar on Andoya-system description and first results. *Radio Science*, 47, 02 2012. doi: 10.1029/2011RS004775.

L. Mearns, F. Giorgi, P. Whetton, J. D. Caicedo, M. Hulme, and M. Lal. Guidelines for use of climate scenarios developed from regional climate model experiments. 01 2003.

NASA. URL https://ccmc.gsfc.nasa.gov/cgi-bin/modelweb/models/vitmo_model.cgi.

R. D. Palmer, S. Gopalam, T.-Y. Yu, and S. Fukao. Coherent radar imaging using capon's method. *Radio Science*, 33(6):1585–1598, 1998. doi: 10.1029/98RS02200. URL https://agupubs.onlinelibrary.wiley.com/doi/abs/10.1029/98RS02200.

M. Parker and A. Corporation. Radar basics - chapter 4: Space-time adaptive processing, Jun 2011. URL https://www.eetimes.com/document.asp?doc_id=1278878#.

J. Picone, A. Hedin, D. Drob, and A. Aikin. NRLMSISE-00 empirical model of the atmosphere: Statistical comparison and scientific issues. *Journal of Geophysical Research*, 107, 12 2002. doi: 10.1029/2002JA009430.

R. A. Pielke. The atmospheres of other planets 2019, jan 2019. URL `https://www.britannica.com/science/atmosphere/Cloud-research#ref952979`.

Rapp and Lübken. Polar Mesosphere Summer Echoes (PMSE): Review of observations and current understanding. *Atmospheric Chemistry and Physics Discussions*, 4, 12 2004. doi: 10.5194/acpd-4-4777-2004.

T. Renkwitz, G. Stober, R. Latteck, W. Singer, and M. Rapp. New experiments to validate the radiation pattern of the Middle Atmosphere Alomar Radar System (MAARSY). *Advances in Radio Science*, 07 2013. doi: 10.5194/ars-11-283-2013.

R. Rüster, P. Czechowsky, G. Schmidt, and K. Labitzke. VHF radar observations in the stratosphere and mesosphere during a stratospheric warming. *Journal of Atmospheric and Terrestrial Physics*, 45(2):161 – 168, 1983. ISSN 0021-9169. doi: https://doi.org/10.1016/S0021-9169(83)80020-8. URL `http://www.sciencedirect.com/science/article/pii/S0021916983800208`.

K. Sato, M. Tsutsumi, T. Sato, T. Nakamura, A. Saito, Y. Tomikawa, K. Nishimura, M. Kohma, H. Yamagishi, and T. Yamanouchi. Program of the antarctic syowa mst/is radar (pansy). *Journal of Atmospheric and Solar-Terrestrial Physics*, 118:2 – 15, 2014. ISSN 1364-6826. doi: https://doi.org/10.1016/j.jastp.2013.08.022. URL `http://www.sciencedirect.com/science/article/pii/S1364682613002447`. Recent progress from networked studies based around MST radar.

D. E. Siskind, A. W. Merkel, D. R. Marsh, C. E. Randall, M. E. Hervig, M. G. Mlynczak, and J. M. Russell III. Understanding the effects of polar mesospheric clouds on the environment of the upper mesosphere and lower thermosphere. *Journal of Geophysical Research: Atmospheres*, 2018. doi:

10.1029/2018JD028830. URL https://agupubs.onlinelibrary.wiley.com/doi/abs/10.1029/2018JD028830.

E. K. Smith and S. Weintraub. The constants in the equation for atmospheric refractive index at radio frequencies. *Proceedings of the IRE*, 41(8):1035–1037, Aug 1953. doi: 10.1109/JRPROC.1953.274297.

S. Sommer and J. L. Chau. Patches of polar mesospheric summer echoes characterized from radar imaging observations with MAARSY. *Annales Geophysicae*, 34(12):1231–1241, 2016. doi: 10.5194/angeo-34-1231-2016. URL https://www.ann-geophys.net/34/1231/2016/.

G. Stober, S. Sommer, C. Schult, R. Latteck, and J. L. Chau. Observation of Kelvin-Helmholtz instabilities and gravity waves in the summer mesopause above Andenes in Northern Norway. *Atmospheric Chemistry and Physics*, 18(9):6721–6732, 2018. doi: 10.5194/acp-18-6721-2018. URL https://www.atmos-chem-phys.net/18/6721/2018.

M. Urco, J. Chau, T. Weber, and R. Latteck. Enhancing the spatiotemporal features of Polar Mesosphere Summer Echoes PMSE using coherent MIMO and radar imaging at MAARSY. *Atmospheric Measurement Techniques*, 12:955–969, 02 2019. doi: 10.5194/amt-12-955-2019.

J. S. Van Baelen, A. D. Richmond, T. Tsuda, S. K. Avery, S. Kato, S. Fukao, and M. Yamamoto. Radar interferometry technique and anisotropy of the echo power distribution: First results. *Radio Science*, 26(5):1315–1326, 1991. doi: 10.1029/91RS01230. URL https://agupubs.onlinelibrary.wiley.com/doi/abs/10.1029/91RS01230.

Wikipedia contributors. Phase-comparison monopulse — Wikipedia, the free encyclopedia, 2018. URL https://en.wikipedia.org/w/index.php?title=Phase-comparison_monopulse&oldid=847754351. [Online; accessed 17-October-2019].

Wikipedia contributors. Bragg's law — Wikipedia, the free encyclopedia, 2019. URL https://en.wikipedia.org/w/index.php?title=Bragg%27s_law&oldid=921744939. [Online; accessed 18-October-2019].

R. F. Woodman. Coherent radar imaging: Signal processing and statistical properties. *Radio Science*, 32(6):2373–2391, 1997. doi: 10.1029/97RS02017. URL https://agupubs.onlinelibrary.wiley.com/doi/abs/10.1029/97RS02017.

R. F. Woodman and A. Guillen. Radar Observations of Winds and Turbulence in the Stratosphere and Mesosphere. *Journal of Atmospheric Sciences*, 31(2):493–505, Mar 1974. doi: 10.1175/1520-0469(1974)031<0493:ROOWAT>2.0.CO;2.

M. K. Yamamoto, M. Oyamatsu, T. Horinouchi, H. Hashiguchi, and S. Fukao. High time resolution determination of the tropical tropopause by the equatorial atmosphere radar. *Geophysical Research Letters*, 30(21), 2003. doi: 10.1029/2003GL018072. URL https://agupubs.onlinelibrary.wiley.com/doi/abs/10.1029/2003GL018072.

Apendix

A Brightness distribution of Capon method

The equation used for Capon method as derived from the described condition to minimize the brightness in all direction, to expect a particular direction of k. the solution for the minimization of problems are derived mathematical way.

$$min_w B(k,f)e^H w = 1. \tag{1}$$

where,

$$e = \begin{bmatrix} e^{jk.D_1} & e^{jk.D_2} & \dots & e^{jk.D_n} \end{bmatrix}^T \tag{2}$$

The linear solution term e^Hw can be viewed as spatial frequency response in the direction of k.

This issue can be solved by applying Lagrange multiplier, by using the general form of the brightness distribution Palmer et al. [1998].

$$B(k,f) = w^H V(f) w \tag{3}$$

can be rewritten as,

$$L(w,\alpha) = w^H V(f) w + \alpha(e^H w - 1) \tag{4}$$

where α is Lagrange multiplier. If V is positive and definite, the required condition to reduce the problem is given in Equ. 7.1. for the given weight vector w.

$$\frac{d}{dw}L(w,\alpha) = 0 \tag{5}$$

by calculating the gradient we can derive,

$$2V_w + \alpha e = 0 \tag{6}$$

The weight vector which reduces Lagrange is then given as follows.

$$w = \frac{-\alpha e}{2V} \tag{7}$$

by substituting Euq. 7.6 in Equ. 7.1. we get,

$$\alpha = \frac{-2}{e^H V^{-1} e} \tag{8}$$

In conclusion, the optimal weight vector is found to have.

$$w_c = \frac{V^{-1} e}{e^H V^{-1} e} \tag{9}$$

The Brightness distribution can be derived using capon method will be obtained by substituting w_c in Equ. 7.3 we get,

$$B_c(k,f) = \frac{1}{e^H V^{-1} e} \tag{10}$$

we must assume that V is Positive definite, which holds the case for the cross spectral matrix. The B_c(k,f) can be applied to any data, irrespective to the expected structure of the Brightness distribution.

B Data analysed for the summer season 2018

For theses days the raw data has been analyzed, the conversation of the raw data to readable format (cross spectra) is a time consuming task. While one should access the raw data from the magnetic tapes to the online drive. Also we can not copy continuous days of raw data huge in space. Two configuration SIMO and MIMO, Capon method was implemented for all cross spectra, since its does not demands much computational compared to Max-Ent.

B.1 System description and Data availability

The task are performed in the high performance computer with remotely connected to the local machine, i5 processor with 20 cores. python 2.7 software language is used.

Files	June	July	Total
Raw data	611 Gb	625 Gb	1.2 Tb
Cross spectra	182 Gb	196 Gb	378 Gb
Imaging + Plots	29 Gb	32 Gb	61 Gb

Table 1: Analysed data and space.

From the experimental configuration for generation of cross spectra has number of coherent integration is 1, number of fft points is 128 and number of incoherent integration is 16. If the total number of integration period were increased then total number of data points were lost by averaging. So, one should be optimized to choose the number of fft points for the unsophisticated source stutterer.

B.2 Computational time

To generate the cross spectra for 60 sec needs 5 minutes and for imaging Capon MIMO is much faster with better results. on the other hand, Max-Ent demands computationally longer period of time. For instance to analysis of 60 sec of data , Max-Ent demands 20 minutes and 4 hours and 30 minutes for SIMO and MIMO.so we implemented Max-Ent for the special Events analysis purpose.

June	Time	Cross Spectra	Capon		Max-Ent	
			SIMO	MIMO	SIMO	MIMO
1^{th}	11:00 - 13:00	X	X	X	X	
08^{th}	13:00 - 16:00	X	X	X	X	13:00-14:00
15^{th}	13:00 - 16:00	X	X	X	X	
18^{th}	10:00 - 13:00	X	X	X	X	
19^{th}	06:00 - 17:00	X	X	X	X	X
20^{th}	09:00 - 12:00	X	X	X		
21^{th}	10:00 - 13:00	X	X	X		
23^{rd}	07:00 - 13:00	X	X	X		
26^{th}	08:00 - 10:00	X	X	X		
27^{th}	10:00 - 15:00	X	X	X		
29^{th}	11:00 - 15:00	X	X	X	X	

Table 2: Analyzed data for June 2018

July	Time	Cross Spectra	Capon		Max-Ent	
			SIMO	MIMO	SIMO	MIMO
1^{th}	11:00 - 13:00	X	X	X	X	
06^{th}	00:00 - 05:00	X	X	X	X	13:00-14:00
07^{th}	10:00 - 14:00	X	X	X	X	
12^{th}	08:00 - 14:00	X	X	X	X	
15^{th}	14:00 - 19:00	X	X	X	X	X
17^{th}	10:00 - 15:00	X	X	X		
20^{th}	09:00 - 13:00	X	X	X		
21^{rd}	05:00 - 09:00	X	X	X		
25^{th}	00:00 - 02:16	X	X	X		
29^{th}	10:00 - 17:00	X	X	X	X	

Table 3: Analyzed data for July 2018

C RTDI, keogram for different examples

C.1 More figures

The following figures are derived by implementing the Capon's method for the event 2. with different examples of RTDI, keogram for north-south and keogram for east-west direction vs. time.

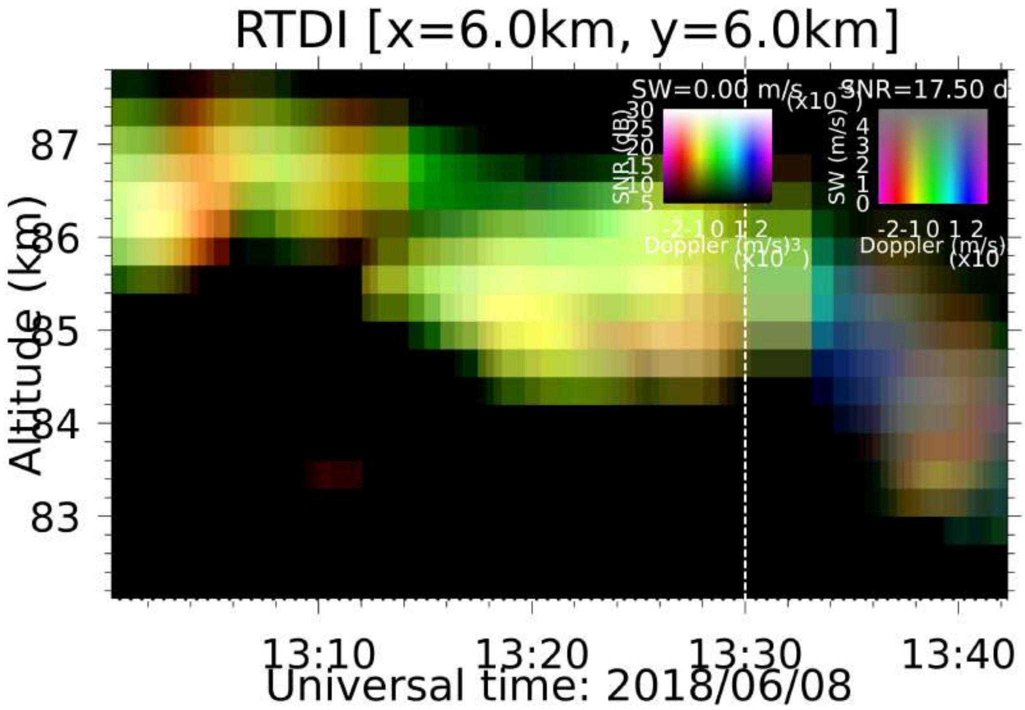

Figure 1: The Range Time Doppler Intensity (RTDI) plot of PMSE using MIMO Capon for time vs. altitude in km. The white doted lines represent the vertical time cut for 13:30:00 UT. The signal intensity is represented as lightness,Doppler information as hue and spectral width as saturation

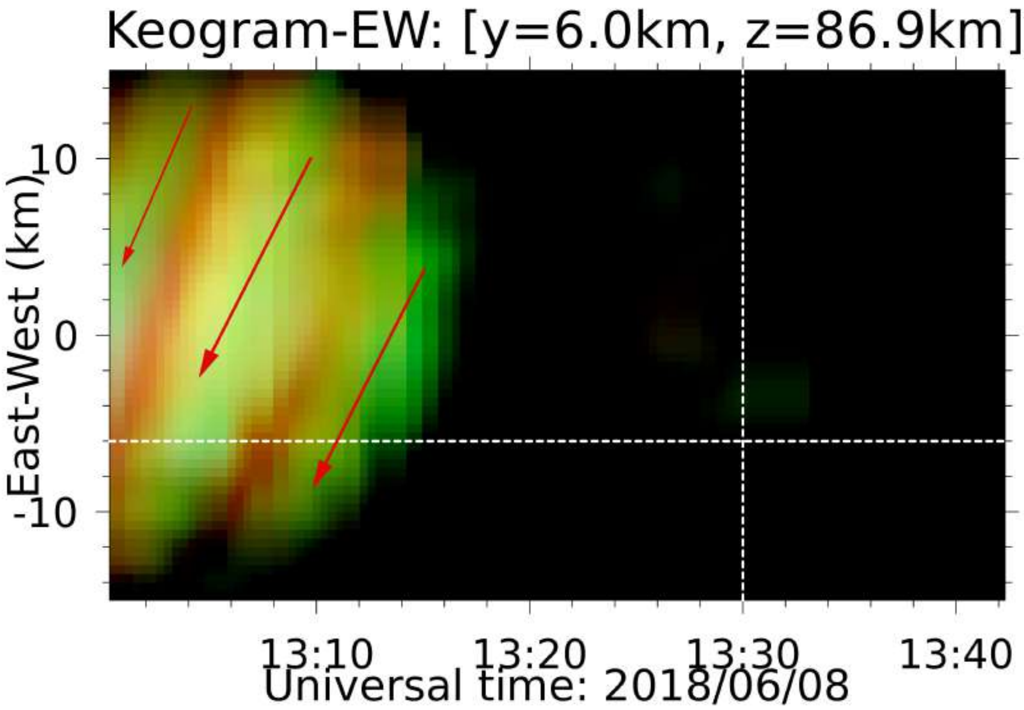

Figure 2: Keogram image for Capon MIMO keogram EW at 2018 June 08^{th} on 13:42:18 UT. The wave like structure moves along the wind in north-west direction

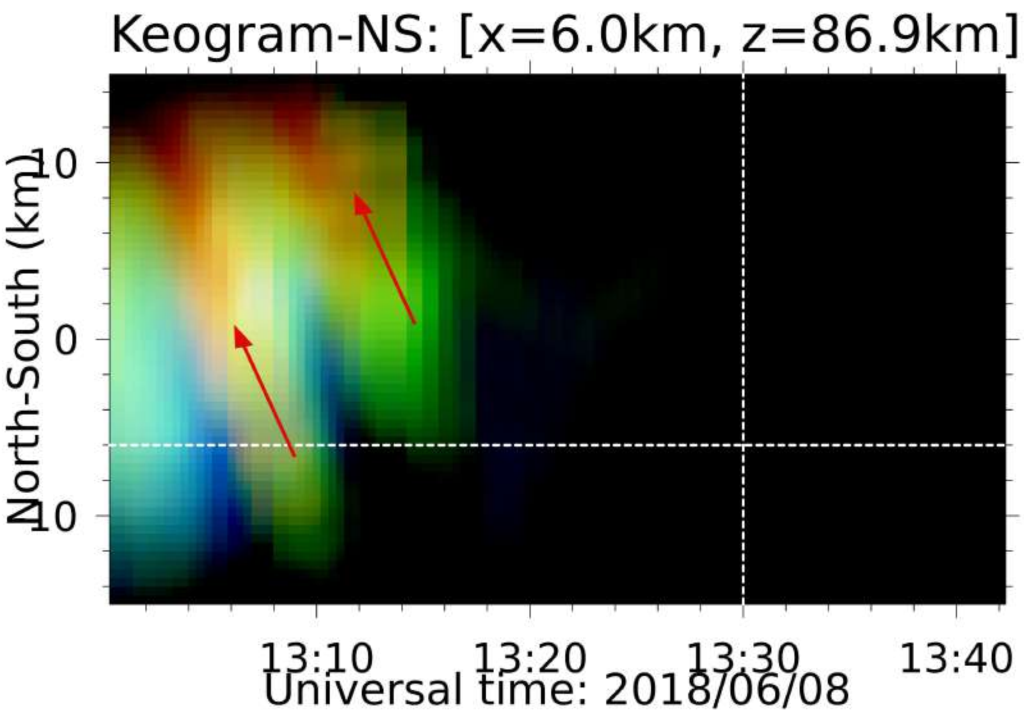

Figure 3: Keogram image for Capon MIMO keogram NS at 2018 June 08^{th} on 13:42:18 UT

C.2 concentric ring structure from imaging

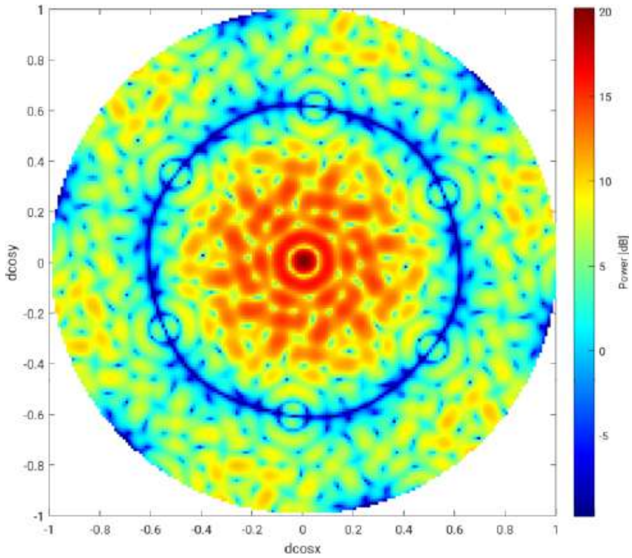

Figure 4: These concentric ringsarise due to the superposition of the receiving channels (receiving hexagons)withthe transmitter pattern approximately 5.5°. This plot was prepared by Dr.Renkwitz

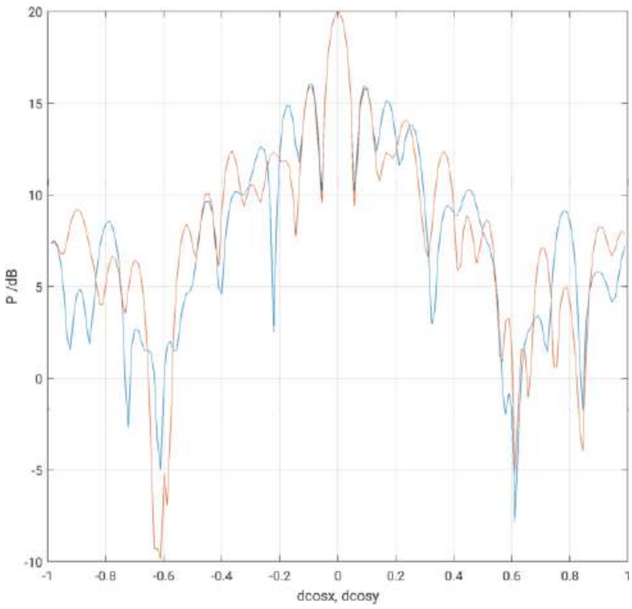

Figure 5: The superposition leads the transmit pattern moves slightly up to + 8 km or - 8 km. This plot was prepared by Dr.Renkwitz

Acknowledgement

It is my privilege to express my sincere regards to Prof. Andreas Ahrens and supervisor Dr.Toralf Renkwitz and Prof. Jorge L. Chau, for offering me this thesis work and I would also like to thank my supervisor Dr.Toralf Renkwitz for his patient guidance, enthusiastic encouragement and useful critiques for this thesis work. I would also like to thank Miguel Urco MSc, PhD scholar. Especially for his advice, providing software and assistance in keeping my progress on schedule. My sincere thanks also extend to Dr. Toralf Renkwitz for his help, for the phase calibration.i also thank Matthias Clahsen MSc. for helping for the radio server access.

I would also like to extend my thanks to the staffs of the Radar department, Leibniz Institute of Atmospheric Physics, Kühlungsborn. For their help in offering me the resources for doing my thesis effectively.

Finally, I wish to thank my parents and friends for their support and encouragement throughout my study.

Statement of Authorship

Hiermit erkläre ich, dass ich dei vorliegende Arbiet selbständig verfasst und keine anderen als die angegebenen Hilfsmilttel benutzt habe. Die Stellen der Arbeit, die anderen Quellen im Wortlaut order dem Sinn nach entnommen wurden, sind durch Angaben der Herkunft kenntlich gemacht. Dies gilt auch für Zeicgnungen, Skizzen, bildiche Darstellungen sowie für Quellen aus dem Internet.
Ich erkläre feerner, dass ich die vorliegende Arbite in keinem anderen Prüfungsverfahren als Prüfungsarbiet eingereicht habe oder einreichen werde.
Die eingereichte schriftliche Fassung entspricht der auf dem Medium gespeicherten Fassung.

Wismar, 17. December 2019 . . . .